

1 Article

2

3 **CTCF-mediated 3D chromatin predetermines the gene expression**

4 **program in the male germline**

5

6 **Yuka Kitamura¹, Kazuki Takahashi², So Maezawa^{2,3}, Yasuhisa Munakata^{1,2}, Akihiko Sakashita^{2,4},**

7 **Noam Kaplan⁵, and Satoshi H. Namekawa^{1,2*}**

8

9

10 ¹ Department of Microbiology and Molecular Genetics, University of California, Davis, Davis, CA,

11 95616, USA.

12 ² Division of Reproductive Sciences, Division of Developmental Biology, Perinatal Institute, Cincinnati

13 Children's Hospital Medical Center, Cincinnati, OH, 45229, USA

14 ³ Faculty of Science and Technology, Department of Applied Biological Science, Tokyo University of

15 Science, Noda, Chiba, 281-8510, Japan.

16 ⁴ Department of Molecular Biology, Keio University School of Medicine, Tokyo, 160-8582 Japan

17 ⁵ Department of Physiology, Biophysics & Systems Biology, Rappaport Faculty of Medicine, Technion -

18 Israel Institute of Technology, Haifa, Israel

19

20 * Corresponding author: E-mail: snamekawa@ucdavis.edu

21 **Abstract**

22

23 **Spermatogenesis is a unidirectional differentiation process that generates haploid sperm, but how**
24 **the gene expression program that directs this process is established is largely unknown. Here we**
25 **determine the high-resolution 3D chromatin architecture of male germ cells during**
26 **spermatogenesis and show that CTCF-mediated 3D chromatin predetermines the gene expression**
27 **program required for spermatogenesis. In undifferentiated spermatogonia, CTCF-mediated**
28 **chromatin contacts on autosomes pre-establish meiosis-specific super-enhancers (SE). These**
29 **meiotic SE recruit the master transcription factor A-MYB in meiotic spermatocytes, which**
30 **strengthens their 3D contacts and instructs a burst of meiotic gene expression. We also find that at**
31 **the mitosis-to-meiosis transition, the germline-specific Polycomb protein SCML2 resolves**
32 **chromatin loops that are specific to mitotic spermatogonia. Moreover, SCML2 and A-MYB**
33 **establish the unique 3D chromatin organization of sex chromosomes during meiotic sex**
34 **chromosome inactivation. We propose that CTCF-mediated 3D chromatin organization enforces**
35 **epigenetic priming that directs unidirectional differentiation, thereby determining the cellular**
36 **identity of the male germline.**

37

Introduction

38

Eukaryotic genomes are folded into a dynamic three-dimensional (3D) architecture within the nucleus that influences gene expression¹⁻⁴. The development of genome-wide chromosome conformation capture methods, especially Hi-C⁵, has accelerated our understanding of the 3D genome and the interplay between 3D genome organization and cell-fate decisions⁶. For example, disruption of 3D chromatin architecture has been shown to lead to disturbed gene expression, incomplete cell differentiation, and conversion to other cell types, at least in cell culture systems^{7,8}. Still, there is a major gap in our understanding of how the 3D genome defines gene expression programs during development and differentiation *in vivo*.

46

47

The mammalian male germline provides an ideal model to decipher the relationship between the 3D genome and gene expression programs. In spermatogenesis, after sex determination, male germ cells undergo a unidirectional differentiation process that comprises the maintenance of spermatogonia stem cells, commitment to meiosis, and production of haploid sperm⁹. Male germ cell differentiation is defined by chromatin-based mechanisms that instruct stage-specific gene expression both on autosomes and on sex chromosomes¹⁰⁻¹². In spermatogonia, histone modifications are preset to regulate later gene expression programs¹³⁻¹⁶. Specifically, on autosomes, dimethylation of histone H3 at lysine 4 (H3K4me2) is pre-established on meiotic super-enhancer (SE) loci that drive a genome-wide burst of transcription after the mitosis-to-meiosis transition¹⁷. The sex chromosomes, on the other hand, undergo meiotic sex chromosome inactivation (MSCI), an essential event in the male germline^{11,18}. They form a distinct nuclear compartment called the XY body (sex body) that is physically segregated from the autosomes¹⁹.

58

59

In this study, we elucidated how the 3D genome architecture of male germ cells is regulated to define the gene expression programs that drive spermatogenesis. Drawing on the recent analysis of basic 3D chromatin features in spermatogenesis²⁰⁻²⁴, we performed high-resolution Hi-C analysis using cell types representative of major stages of spermatogenesis to decipher the detailed pictures of the 3D genome in the male germline at unprecedented resolution. To determine how the 3D genome regulates the dynamic transcriptional transition from the mitotic to meiotic stages, we also performed Hi-C analyses using mouse mutants lacking key transcriptional regulators of spermatogenesis. One of these factors is SCML2, a germ cell-specific component of Polycomb Repressive Complex 1 (PRC1) that is critical for the suppression of the mitotic program in late spermatogenesis². The other is A-MYB (MYBL1), a master transcription factor that regulates the burst of meiotic gene expression at the pachytene stage²⁵. These functional analyses reveal that SCML2 resolves the mitotic 3D chromatin organization, whereas A-MYB drives the establishment of meiotic 3D chromatin. Importantly, we show that the unidirectional differentiation program during spermatogenesis is predetermined by CTCF-mediated 3D chromatin

72 contacts. These results provide a molecular basis for the cellular identity of male germ cells defined by
73 the 3D genome.

74

75 **Results**

76 **High-resolution Hi-C data sets reveal 3D chromatin reprogramming during spermatogenesis**

77 To determine high-resolution 3D chromatin structures of germ cells during the course of
78 spermatogenesis, we performed in-depth Hi-C analysis of spermatogenic cells isolated at four
79 representative developmental stages (Fig. 1a). Specifically, we isolated THY1⁺ undifferentiated
80 spermatogonia and KIT⁺ differentiating spermatogonia from the testes of 7-day-old male C57BL/6 mice
81 using magnetic-activated cell sorting (MACS)²⁶. In addition, we isolated pachytene spermatocytes (PS),
82 which are in the meiotic prophase, and round spermatids (RS), which are in the postmeiotic stage, from
83 the testes of adult male C57BL/6 mice using BSA gradient sedimentation²⁰. We confirmed high purity for
84 all cell types (Extended Data Fig. 1a, b) and performed Hi-C experiments on two biological replicates for
85 each cell type (Supplementary Table 1). These replicates showed a high correlation (Extended Data Fig.
86 1c) and we merged them for downstream analysis, yielding ~430-670 million Hi-C contact reads for each
87 stage and exceeding the total read depths of previous Hi-C analyses in spermatogenesis²⁰⁻²⁴. Comparing
88 the four developmental stages, we detected a relatively high correlation between mitotic spermatogonia
89 (THY1⁺ and KIT⁺) compared to PS and RS (Extended Data Fig. 1d). This reflects the biological similarity
90 between THY1⁺ and KIT⁺ spermatogonia and the presence of a dynamic transition from the mitotic
91 stages to the meiotic and postmeiotic stages.

92

93 Next, we examined the Hi-C maps of an entire representative chromosome (chromosome 7) at
94 each stage, including a zoom-in to a specific chromosomal region (Fig. 1b). Previous high-resolution Hi-
95 C studies in other cellular systems revealed the presence of point interactions that represent stable
96 chromatin-loops (dots) in addition to topologically associating domains (TADs), which manifest in
97 triangular patterns²⁷⁻²⁹. We also detected these stable chromatin loops ("chromatin loops" hereafter) (Fig.
98 1b, bottom, marked by circles), confirming the high resolution of our new data sets. The Hi-C interaction
99 contact matrices show that the genomes of THY1⁺ and KIT⁺ cells are enriched in distal interactions (>10
100 Mb), a typical feature of interphase nuclei. These interactions are abolished in PS, where proximal
101 interactions (a range between 1-10 Mb) dominate (Fig. 1b). This tendency was confirmed by a contact
102 probability $P(s)$ analysis, which is indicative of the general polymer state of chromatin^{5,30} (Fig. 1c). These
103 results corroborate previous Hi-C studies^{21,22} and confirm that the typical interphase pattern of high-order
104 chromatin present in spermatogonia is reprogrammed when cells enter meiosis.

105

106 **Formation of inter-TAD chromatin loops for meiotic gene regulation**

107 Chromatin is spatially organized into TADs, which restrict interactions of cis-regulatory
108 sequences and thereby contribute to gene regulation³¹⁻³³. Accordingly, chromatin loops, which are critical
109 for gene expression regulation^{1,34,35}, are typically observed within TADs. Indeed, in THY1⁺
110 spermatogonia, chromatin loops were largely detected within TADs (intra-TADs: Fig. 1d). By contrast, in
111 PS, many chromatin loops were detected beyond TAD borders (inter-TADs, Fig. 1d). From mitotic
112 spermatogonia to meiotic PS, the total number of chromatin loops decreased (Fig. 1e). Of note, the
113 chromatin loops present in THY1⁺ spermatogonia and PS are mostly unique, and the same holds true for
114 the subsequent PS to RS transition (Fig. 1f). This feature presumably reflects formation and resolution of
115 meiotic chromosome structure, organized into chromatin loop arrays along chromosome axes. Moreover,
116 the length of chromatin loops increased from mitotic spermatogonia to meiotic PS (Fig. 1g), while
117 average contact strengths decreased based on a pile-up analysis³⁶ (Fig. 1h). These results demonstrate that
118 the structural changes that occur at the mitosis to meiosis transition are based on the resolution of intra-
119 TAD chromatin loops and the de novo establishment of inter-TAD chromatin loops.
120

121 The weakening of TADs in PS²⁰⁻²⁴ indicates that this feature might drive meiotic gene regulation
122 mediated by inter-TAD chromatin loops. To test this possibility, we investigated the relationship between
123 TAD strength and chromatin loop formation during spermatogenesis. First, we detected TADs in each
124 stage of spermatogenesis. The number of TADs decreased during the transition from spermatogonia to
125 meiotic PS and recovered in postmeiotic RS (Fig. 2a). This is consistent with previous reports showing
126 the attenuation of TADs in meiotic prophase^{21,22}. TAD boundaries were largely shared between THY1⁺
127 and KIT⁺ spermatogonia, with 3,550 common TAD boundaries (85% of 4,192 THY1⁺ TAD boundaries),
128 and they progressively changed from KIT⁺ to PS and from PS to RS (Fig. 2b). Among 4,039 TAD
129 boundaries in KIT⁺ spermatogonia, only 1,447 (36%) were maintained in PSs. In contrast, from PSs to
130 RSs, 1,935 (80%) out of 2,420 PS TAD boundaries were maintained, and 1,659 TAD boundaries were
131 newly generated in RS (Fig. 2b). To define stage-specific features of TADs, we next examined the
132 average contact strength of TADs using a pile-up analysis of the Hi-C matrices, which visualizes average
133 insulation strengths of the regions around TADs and their boundaries³⁶. We found that while insulation at
134 TAD boundaries was weakened during the transition from KIT⁺ spermatogonia to PS (Fig. 2c), the
135 interaction strengths between adjacent TADs increased (Fig. 2d). Thus, during the transition from mitotic
136 spermatogonia to meiotic PS, TADs and TAD borders are reprogrammed. Interactions beyond TAD
137 boundaries increase in meiosis, not only through the de novo formation of inter-TAD chromatin loops but
138 also through TAD-TAD interactions.
139

140 There are various types of chromatin loops, including CTCF-CTCF loops, enhancer-promoter
141 loops, and Polycomb-dependent loops. Since these different types contribute to gene activation or

142 silencing^{28,37}, it is possible to infer their functions. Therefore, we examined the modifications on anchor
143 sites of chromatin loops and distinguished the three loop classes based on the presence of CTCF,
144 H3K4me3 (a promoter mark)/H3K27ac (an active enhancer mark), or H3K27me3 (the Polycomb
145 repressive complex2 (PRC2)-mediated mark). First, we performed CTCF ChIP-seq in THY1⁺
146 spermatogonia and PS (Extended Data Fig. 2a). CTCF binding sites overlapped with 35.6% of anchor
147 sites of THY1⁺ chromatin loops, while this overlap decreased to 17.3 % in PS, suggesting the resolution
148 of CTCF-pair loops during meiosis (Fig. 2e). Indeed, at some of the sites of CTCF-pair loops in THY1⁺
149 spermatogonia, CTCF enrichment was reduced or lost in PS (Fig. 2f). This suggests that the loss of CTCF
150 might underly the resolution of some CTCF-pair loops in meiosis. Second, we used our previous
151 H3K4me3, H3K27ac, and H3K27me3 ChIP-seq datasets in THY1⁺ and PSs^{17,38,39} and defined
152 enhancer/promoter-pair loops and Polycomb-dependent loops. The proportion of enhancer/promoter-pair
153 loops was in the range of ~20-30 %, and the proportion of Polycomb-dependent loops was less than 10 %
154 of total chromatin loops in THY1⁺ and PS (Fig. 2e). Since chromatin loops in PS are mostly PS-specific
155 (Fig. 1f), all three types of chromatin loops are largely de novo generated during meiosis. Contact
156 strengths were comparable within each class of loops in THY1⁺ and PS (Extended Data Fig. 2b),
157 indicating that contact strength is not class- but stage-dependent.

158
159 We further examined how the resolution of TADs at the mitosis-to-meiosis transition is regulated.
160 As opposed to the resolution of CTCF-pair loops (Fig. 2e, f), there was no change in the proportion of
161 CTCF-associated TAD boundaries among all TAD boundaries (Extended Data Fig. 2c). This suggests
162 that distinct mechanisms operate between the resolution of TAD boundaries and chromatin loops in
163 meiosis. Taken together, these results demonstrate that attenuation of TADs and resolution of CTCF-pair
164 loops take place at the mitosis-to-meiosis transition to establish long inter-TAD loops during meiosis
165 (Fig. 2g).

166 167 **SCML2 is required for the resolution of spermatogonia-type 3D chromatin and gene repression**

168 To further understand the mechanisms that underlie the resolution of TAD boundaries and
169 chromatin loops at the transition from mitotic spermatogonia to meiotic spermatocytes, we focused on the
170 germline-specific Polycomb protein SCML2. SCML2 is responsible for the suppression of genes that are
171 highly expressed in mitotic spermatogonia after the mitosis-to-meiosis transition¹⁴. It is expressed in
172 undifferentiated spermatogonia and forms part of PRC1, which deposits H2AK119ub¹⁴ and facilitates
173 PRC2-mediated H3K27me3 during meiosis³⁹. H3K27me3 counteracts the active enhancer mark
174 H3K27ac, thereby resolving spermatogonia-type enhancers¹⁷. We therefore hypothesized that SCML2 is
175 involved in the resolution of spermatogonia-type 3D chromatin. To test this hypothesis, we performed Hi-
176 C analysis using *Scml2* knockout (*Scml2*-KO) PSs and RSs (Extended Data Fig. 1c). *Scml2*-KO PSs and

177 RSs showed increased distal interactions compared to wild-type cells, and this pattern resembles Hi-C
178 maps in THY1⁺ and KIT⁺ cells (Fig. 3a). Pearson correlation analysis also showed that *Scml2*-KO PSs
179 and RSs are more similar to wild-type THY1⁺ and KIT⁺ than wild-type PSs and RSs (Extended Data Fig.
180 1d). This suggests that the mitotic 3D chromatin organization of spermatogonia is retained in *Scml2*-KO
181 cells during meiosis.

182
183 To determine whether SCML2 mediates the resolution of spermatogonia-type TAD boundaries,
184 we detected TADs in the Hi-C dataset of *Scml2*-KO PS and RS. The number of TADs increased in *Scml2*-
185 KO PS compared to wild-type PS (Fig. 3b). Of note, TAD boundaries in the *Scml2*-KO PSs overlapped
186 with the TAD boundaries in wild-type KIT⁺ spermatogonia at 2,523 loci (Fig. 3c). This overlap is more
187 abundant than that between KIT⁺ and wild-type PS TAD boundaries (1,447 loci; Fig. 3c), suggesting that
188 spermatogonia-type TAD boundaries are retained in *Scml2*-KO PS. Indeed, among 2,613 KIT⁺-specific
189 TAD boundaries (which do not overlap with wild-type PS TAD boundaries), 1,191 loci remain in *Scml2*-
190 KO PS TAD boundaries. Pile-up analysis further confirmed that KIT⁺-specific TAD boundaries remain in
191 *Scml2*-KO PS (Fig. 3d). These results indicate that SCML2 is required for the resolution of KIT⁺-specific
192 TADs in PS.

193
194 Next, we examined the role of SCML2 in the resolution of chromatin loops. The number of
195 chromatin loops increased in *Scml2*-KO PSs and RSs compared to wild-type PS and RS (Fig. 3e). While
196 wild-type KIT⁺-specific chromatin loops did not show high contact strengths in wild-type PS and RS,
197 they remained in *Scml2*-KO PS and RS (Fig. 3f). On the other hand, chromatin loops detected in wild-
198 type PS and RS did not show high contact strengths in *Scml2* KO PS and RS (Fig. 3f). Comparison of
199 chromatin loops between wild-type PSs and *Scml2*-KO PSs revealed that there were 1,358 *Scml2*-KO-
200 specific chromatin loops, 677 of which are shared with chromatin loops present in wild-type KIT⁺ (Fig.
201 3g). The persistence of KIT⁺ chromatin loops in *Scml2* KO PS and RS was confirmed with Hi-C maps
202 (Extended Data Fig. 3a). Therefore, SCML2 is also involved in the resolution of spermatogonia-type
203 chromatin loops.

204
205 To determine how SCML2 resolves spermatogonia-type 3D chromatin, we next examined
206 whether SCML2 is required for the resolution of CTCF sites by performing CTCF ChIP-seq in *Scml2*-KO
207 PS. The Pearson correlation between *Scml2*-KO PS and wild-type THY1⁺ spermatogonia (0.79) is higher
208 than the Pearson correlation between wild-type PS and wild-type THY1⁺ (0.73; Extended Data Fig. 3c),
209 suggesting that CTCF distribution in *Scml2*-KO PS is more similar to wild-type THY1⁺ than that in wild-
210 type PS. In wild-type PS, CTCF enrichment at the anchor sites of the CTCF pair loops detected in THY1⁺

211 was reduced (Fig. 2f), but CTCF enrichment at these loci remained high in *Scml2*-KO PS (Fig. 3h). This
212 suggests that SCML2 is involved in the resolution of at least a fraction of CTCF sites.
213

214 Since chromatin conformation is implicated in the regulation of gene expression^{31,33}, we
215 examined the effect of the KIT⁺-specific loops that persist in *Scml2*-KO PS on gene expression.
216 Therefore, we examined the expression profile of 1,243 genes present in the anchor sites of the *Scml2*-KO
217 PS-specific loops defined in Fig. 3g. The overall expression level of these genes decreased from wild-type
218 KIT⁺ to wild-type PSs, but remained high in *Scml2*-KO PS compared to wild-type PSs (Fig. 3i). We thus
219 conclude that SCML2 is required for the resolution of spermatogonia-type 3D chromatin, thereby
220 suppressing spermatogonia-type gene expression in meiosis (Fig. 3j). Importantly, we did not observe a
221 significant change in contact strengths of chromatin loops at SCML2-dependent bivalent promoters
222 marked by both active (H3K4me2/3) and repressive (H3K27me3) histone modifications (Extended Data
223 Fig. 3d). Therefore, the function of SCML2 in resolving spermatogonia-type 3D chromatin is independent
224 of its regulation of bivalent promoters³⁹.
225

226 **A-MYB is required for the formation of meiotic-type 3D chromatin and gene activation**

227 Because meiosis-specific chromatin loops are *de novo* generated after the resolution of
228 spermatogonia-type chromatin loops (Fig. 2g), we next sought to determine the mechanism driving
229 meiosis-specific chromatin loops. To this end, we focused on A-MYB, a transcription factor responsible
230 for the activation of pachytene-specific genes²⁵. A-MYB is required to establish H3K27ac on pachytene-
231 specific enhancers, thereby activating these enhancers¹⁷. We suspected a role of A-MYB in the formation
232 of meiosis-specific chromatin loops because of the establishment of specific enhancer/promoter-pair
233 loops in PS. We therefore isolated PS from *A-myb* mutant (*Myb1I*^{repro9}) mice and performed Hi-C
234 analysis. We found that distal interactions were increased in the *A-myb* mutant PS as shown in a Hi-C
235 heat map (Fig. 4a) and in a contact probability analysis (Extended Data Fig. 4a), suggesting that
236 spermatogonia-type 3D chromatin is retained in the *A-myb* mutant PS. In accordance with this notion, the
237 number of TADs also increased (Fig. 4b); in fact, more than 70% of the TAD boundaries in the *A-Myb*
238 mutant PS were common to those detected in KIT⁺ (Fig. 4c: left), and KIT⁺-specific loops largely
239 remained in the *A-myb* mutant PS (Fig. 4c: right). Further, KIT-specific TAD boundaries retained high
240 contact strength in the *A-myb* mutant PS (Fig. 4d). These results demonstrate that A-MYB is required for
241 the establishment of meiosis-type 3D chromatin, and that its loss leads to the retention of spermatogonia-
242 type 3D chromatin.
243

244 We next examined whether A-MYB is required to establish meiosis-specific chromatin loops.
245 Although the total number of chromatin loops increased in the *A-myb* mutant PS compared to wild-type

246 PS, only 29 % of wild-type PS-specific chromatin loops (357 out of 1,223) were detected in the *A-myb*
247 mutant PS. Pile-up analyses show that *A-myb* mutant PS retained the contact strength of KIT⁺ chromatin
248 loops (Fig. 4f, left), while *A-myb* mutant PS did not show high contact strength for PS chromatin loops
249 (Fig. 4f). To test whether A-MYB directly mediates the formation of chromatin loops in PS, we
250 reanalyzed previous ChIP-seq data of A-MYB using whole testis²⁵. A-MYB is enriched at the anchor sites
251 of PS chromatin loops (Fig. 4g), and A-MYB binds to 41% of genes at anchor sites of PS (849 out of
252 2,092; Fig. 4h). This association is statistically significant when compared to the ratio of all A-MYB
253 binding genes to all RefSeq genes (5,929/22,661; $P = 8.5 \times 10^{-59}$, Hypergeometric test). These results
254 indicate that A-MYB mediates the formation of a large part of chromatin loops in PS (Fig. 4i).

255

256 **A-MYB-dependent 3D chromatin is associated with the production of pachytene piRNAs.**

257 Another major function of A-MYB is the production of pachytene piRNAs⁴⁰, which are involved
258 in the maintenance of genome integrity and gene regulation in late spermatogenesis^{41,42}. A-MYB drives
259 the production of pachytene piRNAs in a parallel mechanism with its regulation of enhancers through the
260 induction of H3K27ac at pachytene piRNA clusters¹⁷. The loci of pachytene piRNA clusters switch from
261 the B compartment to the A compartment during the mitosis-to-meiosis transition²². Our Hi-C data
262 showed that 3D chromatin contacts were specifically detected at pachytene piRNA clusters in PS and
263 were retained in RS, and that the formation of 3D chromatin is A-MYB dependent (Extended Data Fig.
264 4b). Thus, the A-MYB-mediated formation of 3D chromatin is associated with the production of
265 pachytene piRNAs.

266

267 **Meiotic super-enhancers are poised within 3D chromatin.**

268 We next sought to determine how the global transcriptional changes that occur during
269 spermatogenesis are regulated in the context of the 3D genome. To address this question, we focused on
270 super-enhancers (SEs), which are long stretches of enhancers that play a central role in driving cell-type-
271 specific gene expression and determining cellular identities⁴³⁻⁴⁵. In PS, A-MYB activates meiosis-specific
272 SEs (meiotic SEs) through the establishment of H3K27ac to drive the expression of late spermatogenesis-
273 specific genes¹⁷. Based on the specific enrichment of H3K27ac, we defined 399 meiotic SEs on
274 autosomes, which are specific to PS. Among these, 270 (67.7%) are associated with PS chromatin loops
275 (Extended Data Fig. 5a). A chromosome-wide track view confirms that chromatin loops (detected as
276 stable chromatin loops in this study) are largely associated with SEs and the active genic loci that are in
277 context with SEs (Fig. 5a). Therefore, these stable chromatin loops are associated with gene regulation
278 and are distinct from meiotic chromatin loop arrays that are formed along the chromosome axes during
279 meiotic prophase⁴⁶.

281 We also defined 107 “mitotic” SE that are specific to THY1⁺ and KIT⁺ spermatogonia and found
282 that mitotic SEs and meiotic SEs exhibited distinct 3D chromatin dynamics during spermatogenesis. At
283 the mitotic SE loci, strong 3D contacts were detected in THY1⁺ and KIT⁺ spermatogonia, which resolved
284 together with the resolution of mitotic SEs in PS and RS (Fig. 5b). On the other hand, at meiotic SE loci,
285 3D chromatin contacts were detected in THY1⁺ and KIT⁺ spermatogonia prior to the establishment of
286 meiotic SEs and increased upon activation of meiotic SEs in PS (Fig. 5c). Pre-establishment of 3D
287 contacts of meiotic SEs in KIT⁺ was also detected in a representative Hi-C map (Extended Data Fig. 5b).
288 These 3D contacts cover relatively large regions and are distinct from chromatin loops that are detected as
289 local point interactions. To further analyze the 3D chromatin structure around the meiotic SEs, we
290 detected Hi-C interacting loci centered around the meiotic SEs (Extended Data Fig. 5c). A pile-up
291 analysis shows that, consistent with the SE-SE interactions, contact strength of Hi-C interacting loci
292 increase in PS, while modest contacts are already present in mitotic spermatogonia (Extended Data Fig.
293 5d). These results suggest that 3D contacts at meiotic SEs are preprogrammed in spermatogonia, raising
294 the possibility that meiotic SEs are poised for later activation through 3D chromatin.
295

296 Because SEs determine cell type-specific gene expression programs, we next sought to determine
297 how meiotic SEs regulate target genes via 3D chromatin. We detected 611 genes that are overlapping
298 with the genomic region interacting with meiotic SEs. Among these genes, 26 genes are associated with
299 the GO term spermatogenesis, and were largely upregulated in PSs and RSs (Extended Data Fig. 6a and
300 b). In our previous study, we showed that spermatogenesis-related genes adjacent to the meiotic SEs are
301 upregulated during late spermatogenesis¹⁷. Here, we extend this observation by demonstrating that
302 meiotic SEs also upregulate SE-interacting genes via 3D contacts.
303

304 Next, to investigate how meiotic SEs regulate gene expression, we examined the epigenetic states
305 of genes adjacent to meiotic SE and SE-interacting loci. H3K4me2, which is implicated in the poised
306 chromatin state¹⁵ and associated with poised meiotic SEs¹⁷, accumulated highly at these genes in KIT⁺
307 spermatogonia, but decreased in PS upon activation of meiotic SEs (Extended Data Fig. 6c, d). In PS,
308 H3K4me3 and H3K27ac, markers for active promoters and enhancers, are enriched at these loci instead.
309 Together, these results suggest that meiotic SE pre-establish H3K4me2-enriched 3D contacts with target
310 genes in mitotic spermatogonia, and this epigenetic state is reprogrammed to an H3K4me3/H3K27ac-
311 enriched state upon activation of meiotic SEs.
312

313 **CTCF predetermines the 3D contacts of the meiotic SEs in spermatogonia**

314 To determine how the 3D contacts of the meiotic SE are predetermined in spermatogonia, we
315 focused on CTCF, which is involved in mediating 3D chromatin contacts via CTCF-CTCF

316 interactions^{47,48}. To examine the relationship between CTCF and meiotic SEs, we extracted 844 CTCF-
317 binding sites that overlapped with meiotic SEs and their interacting genomic regions in PS (Fig. 5d). We
318 also identified 13,690 sites that did not overlap with those genomic regions (Extended Data Fig. 7a).
319 CTCF enrichment was largely maintained at the 844 CTCF binding sites that overlapped with meiotic
320 SEs from THY1⁺ spermatogonia to PS (Extended Data Fig. 7b), raising the possibility that CTCF-
321 mediated 3D chromatin contacts persist from mitotic spermatogonia to PS. Indeed, a representative Hi-C
322 heatmap shows that 3D chromatin contacts at the meiotic SE loci are pre-established in THY1⁺
323 spermatogonia and that CTCF is highly enriched at these sites (Fig. 5e). A pile-up analysis confirmed that
324 strong 3D contacts are maintained from THY1⁺ spermatogonia to RS at CTCF binding sites that overlap
325 with meiotic SEs (Fig. 5f). Of note, this feature is specific to SE loci because CTCF-CTCF chromatin
326 loops are largely reprogrammed from THY1⁺ spermatogonia to PS (Fig. 2e). These results demonstrate
327 that CTCF predetermines the 3D contacts of meiotic SEs in spermatogonia, poising them for later
328 activation.

329

330 **A-MYB strengthens 3D contacts of meiotic SEs on autosomes**

331 Because A-MYB establishes meiotic SEs¹⁷, we reasoned that A-MYB strengthens 3D contacts of
332 meiotic SEs in PS. Indeed, a representative track-view shows that A-MYB binds to meiotic SE-
333 interacting loci (Fig. 5g). Specifically, it binds to the promoter regions of 294 of the 611 genes that
334 interact with meiotic SE-interacting loci (48.1%; Extended Data Fig. 7c). To examine the role of A-MYB
335 in the regulation of 3D chromatin at meiotic SEs, we analyzed the Hi-C data of *A-myb* mutant PS. 3D
336 contacts between meiotic SE and the interacting loci were attenuated in the *A-myb* mutant PS compared to
337 wild-type PS, although modest contacts were still observed (Fig. 5h, i). Together with the CTCF analysis,
338 we conclude that there are two regulatory mechanisms for the establishment and maintenance of meiotic
339 SEs: CTCF predetermines the overall 3D contacts of meiotic SEs in mitotic spermatogonia, and A-MYB
340 strengthens these 3D contacts upon activation of meiotic SEs in meiotic spermatocytes (Fig. 5j).

341

342 **SCML2 and A-MYB establish the unique 3D chromatin architecture of the meiotic sex** 343 **chromosomes**

344 During meiosis, sex chromosomes undergo epigenetic programming that is different from
345 autosomes. They are subject to MSCI and form a distinct nuclear compartment called the XY body (also
346 known as the sex body)^{11,18} (Fig. 1a). After meiosis, the silent XY-chromosomal structure, called
347 postmeiotic sex chromatin (PMSC), persists in haploid spermatids⁴⁹. Previous Hi-C studies demonstrated
348 that meiotic sex chromosomes do not show specific 3D chromatin features²⁰⁻²⁴, supporting the notion that
349 3D chromatin structures of the sex chromosomes are random throughout a cell population. In our Hi-C
350 data, we confirmed that spermatogonia-type far-cis interactions disappeared from the X chromosome in

351 PS (Fig. 6a). Although there are 26 meiotic SEs on the X chromosome in wild-type PS (Extended Data
352 Fig. 8a), we did not detect loci that interacted with these meiotic SEs (Extended Data Fig. 8b). We did,
353 however, detect an enrichment of short-range interactions (less than 1.5 Mb) on the X chromosome
354 specifically in PS (Extended Data Fig. 8c-e), which might be related to fact that the X chromosome
355 remains unsynapsed during meiotic prophase I.

356
357 To determine the mechanisms underlying the unique 3D chromatin organization of the X
358 chromosome, we focused on SCML2 and A-MYB. SCML2 is known to accumulate and function on
359 meiotic sex chromosomes, independently and via a distinct mechanism compared to autosomes¹⁴. A-
360 MYB is required to establish chromosome-wide accumulation of H3K27ac on the sex chromosome¹⁷,
361 which facilitates the activation of sex-linked genes in postmeiotic RS³⁸. These functions of SCML2 and
362 A-MYB are regulated downstream of the DNA damage response pathways centered on γH2AX and its
363 binding protein MDC1, which initiate MSCI at the onset of the early pachytene stage^{14,17,50}. In *Scml2*-KO
364 PS, spermatogonia-type far-cis interactions remain on the X chromosome (Fig. 6b, Extended Data Fig.
365 8f), and this feature persists in *Scml2*-KO RS (Extended Data Fig. 8h). In *A-myb* mutant PS,
366 spermatogonia-type far-cis interactions also remain on the X chromosome and we observe a plaid pattern
367 of Hi-C signals, which represents the maintenance of spermatogonia-type compartment strengths (Fig. 6c,
368 Extended Data Fig. 8g). These results indicate that both SCML2 and A-MYB are necessary to establish a
369 unique 3D chromatin organization of the X chromosome.

370
371 Since meiotic sex chromosome are segregated from autosomes through the formation of the XY
372 body, we examined interchromosomal interactions between the X and autosomes. In wild-type PS, these
373 interchromosomal interactions decreased during spermatogenesis (Fig. 6d, Extended Data Fig. 9). In
374 contrast, in *Scml2*-KO and *A-myb* mutant PS, interchromosomal interactions remained (Fig. 6d, Extended
375 Data Fig. 9), indicating that the segregation of the sex chromosomes from autosomes is dependent on
376 SCML2 and A-MYB (Fig. 6f). Interchromosomal interactions between autosomes remain intact in *Scml2*-
377 KO and *A-myb* mutant PS, including the association of pericentromeric heterochromatin and telomeres as
378 well as the overall association of autosomes (represented by “X” shape signals on Hi-C maps as described
379 previously⁵¹) (Fig. 6e). Therefore, the role of SCML2 and A-MYB in regulating interchromosomal
380 interactions of meiotic chromosomes is specific to the interaction between the X chromosome and
381 autosomes (Fig. 6g).

382
383 In summary, we conclude that SCML2 and A-MYB are required for the establishment of the
384 unique 3D chromatin architecture of the sex chromosomes (Fig. 6h) and the formation of the segregated
385 XY body.

386

387

Discussion

388

389

390

391

392

393

394

395

396

397

398

399

400

401

402

403

404

405

406

407

408

409

410

411

412

413

414

415

416

417

418

419

420

In this study, we determined the high-resolution 3D genome architecture of cell types representative of different stages of spermatogenesis and defined regulatory mechanisms underlying the transition from mitotic spermatogonia to meiotic spermatocytes. We demonstrated that, in spermatogonia, CTCF-mediated 3D contacts at meiotic SE are pre-established. Since meiotic SEs instruct the burst of meiotic gene expression, these poised 3D contacts represent a mechanism to maintain the cellular identity of male germ cells during spermatogenesis. Thus, we show that pre-programming through 3D contacts represents a novel feature of epigenetic priming. Of note, the poised 3D contacts in juvenile spermatogonia reflect the gene expression program of meiotic spermatocytes in adult testis, therefore they are maintained for a long time. Such 3D chromatin-based memories are likely to be prevalent in the germline, as sperm 3D chromatin is preset through histone modifications in late spermatogenesis as well²⁰.

Epigenetic priming enables a rapid change in gene expression upon a signaling cue based on a pre-established chromatin state. It has been observed in various biological contexts, including immune cells⁵², neuronal⁵³ and cancer development⁵⁴, as well as during spermatogenesis to instruct the gene expression program in late spermatogenesis¹⁵. Mechanistically, the pre-formation of enhancer-promoter pairs drives transcriptional changes upon differentiation in a variety of organisms and cell types⁵⁵⁻⁵⁷. Pre-formed enhancer-promoter pairs are associated with paused RNA polymerase⁵⁶ and a recent study showed that meiotic transcription bursts in the male germline are associated with the release of paused RNA polymerase, which is mediated by A-MYB and the testis-specific bromodomain protein BRDT⁵⁹. We propose that at meiotic SEs these mechanisms operate in the context of 3D chromatin. In support of this hypothesis, in somatic cells, SEs are driven by another bromodomain protein, BRD4, as well as Mediator to form liquid-like condensates⁶⁰, thereby providing spatial SE organization. In meiotic spermatocytes, BRDT is expressed in lieu of BRD4⁶¹. Thus, it is conceivable that preestablished 3D contacts provide venues for A-MYB and BRDT-driven spatial organization of meiotic SEs via phase separation to instruct the burst of meiotic gene expression (Fig. 7a).

A key question that remains is the timepoint at which the pre-programmed 3D contacts are established during spermatogenesis. Male germ cells acquire the androgenic epigenome in prospermatogonia (also known as gonocytes) prior to birth⁶². Prospermatogonia are arrested at the G₀/G₁ phase of the cell cycle and genome-wide de novo DNA methylation takes place^{63,64}. A recent study has shown that 3D chromatin reprogramming occurs in prospermatogonia⁶⁵. Therefore, it is possible that the 3D contacts necessary for the spermatogenic gene expression program are established in

421 prospermatogonia. Notably, the number of CTCF binding sites is reduced during in vitro differentiation
422 of primordial germ cell-like cells to germline stem cell-like cells⁶⁶, raising the possibility that the
423 androgenic pattern of CTCF binding sites and 3D contacts are reprogrammed in prospermatogonia.
424 CTCFL (also known as BORIS), a paralog of CTCF^{67,68}, is expressed during spermatogenesis, along with
425 CTCF, and some CTCF-binding sites overlap with CTCFL-binding sites⁶⁹. Hence, CTCFL may be
426 involved in the regulation of CTCF and CTCF-mediated 3D chromatin in spermatogenesis.
427

428 When germ cells enter meiosis, cohesin-mediated axial loops are formed along the chromosome
429 axes to promote homolog pairing and recombination. Cytological analyses suggest that an average axial
430 loop length is ~ hundred(s) kb^{46,70} in mice, but the average axial loop lengths estimated from contact
431 probability analyses of previous Hi-C studies^{24,51} is larger (~ 1 Mb). The average length of stable meiotic
432 chromatin loops detected by our Hi-C analysis is also ~ 1 Mb (Fig. 1f). Yet, we show that these stable
433 chromatin loops are associated with transcription and are formed around super-enhancers (Fig. 5a),
434 suggesting that they are distinct from axial loops. Further studies using independent approaches are
435 needed to clarify if axial loop structures are distinct from stable chromatin loops.
436

437 Finally, our study showed that 3D chromatin organization of the sex chromosomes is regulated by
438 SCML2 and A-MYB. After the initiation of MSCI directed by the DDR pathway at the early pachytene
439 stage, SCML2 localizes on the sex chromosome after the mid-pachytene stage¹⁴. At that time, A-MYB
440 regulates chromosome-wide spreading of H3K27ac on the sex chromosome¹⁷, downstream of the DDR
441 factor RNF8⁷¹. RNF8 interacts with the MSCI initiator, MDC1, which functions as a γH2AX binding
442 protein⁵⁰. Therefore, the DDR pathway coordinates both SCML2 and A-MYB-dependent processes on the
443 sex chromosomes (Fig. 6h). Spermatogonia-type 3D chromatin features are retained in the *Scml2*-KO and
444 *A-myb* mutant PS, suggesting that SCML2 and A-MYB are both required for the establishment of 3D
445 chromatin features of the XY body (Fig. 7b). We suggest that SCML2 and A-MYB may work in concert
446 on the sex chromosomes because SCML2 and RNF8 function together in the regulation of histone
447 ubiquitination on meiotic sex chromosomes³⁸. Similar to A-MYB's function on autosomes, A-MYB could
448 drive a phased separated compartment of the sex chromosomes. Of note, this 3D chromatin feature of the
449 male X chromosome in MSCI is distinct from that of the female inactive X chromosome. The inactivated
450 female X chromosome splits into two mega domains bounded by the *Dxz4* locus and forms long-range
451 loop structures called super loops (>7 Mb)²⁷. CTCF binds around the *Dxz4* locus, and this structure is
452 essential for the formation of mega domains and super loops in female cells⁷². This is quite different from
453 the male X chromosome in meiosis, where short-range interactions are increased, and a domain structure
454 is not clearly visible.

455 Overall, our results uncover the mechanisms underlying the organization of the meiotic chromatin
456 structure on both autosomes and sex chromosomes and establish that CTCF-mediated pre-programming
457 drives the burst of autosomal gene expression during male meiosis.

458

459 **Methods**

460 **Animals and germ cell isolation.**

461 Mice were maintained and used according to the guidelines of the Institutional Animal Care and
462 Use Committee (protocol no. IACUC2018-0040) at Cincinnati Children's Hospital Medical Center. Wild-
463 type C57BL/6J mice, *Scml2*-KO mice¹⁴ on the C57BL/6J background, and *A-myb*^{mut/mut} (*Myb1*^{repro9})²⁵ on
464 the C57BL/6J background were used for Hi-C analyses. Spermatogonia were isolated from C57BL/6J
465 wild-type aged 6-8 days through magnetic cell-sorting (MACS) as described previously²⁶. Pachytene
466 spermatocytes and round spermatids, including *Scml2*-KO PS, *Scml2*-RS, and *A-myb* mutant PS, were
467 isolated from adult testes through sedimentation velocity at unit gravity as described previously^{26,39,73}.

468

469 **Hi-C library generation and sequencing.**

470 To generate and sequence Hi-C libraries, Hi-C was used using the Arima Hi-C kit, according to
471 the manufacturer's instructions. We used the Arima-Hi-C kit, which enables high-resolution detection of
472 3D chromatin by using a combination of multiple restriction enzymes. 4×10^5 to 1×10^6 cells were used for
473 THY1⁺ and KIT⁺, 3×10^6 cells were used for WT PS, *Scml2*-KO PS, and *A-myb* mutant PS, and 4×10^6
474 cells were used for WT RS and *Scml2*-KO RS for crosslinking. For library preparation, Accel-NGS[®] 2S
475 Plus DNA Library Kit (Swift Biosciences, Inc. Ann Arbor, MI) was used. All libraries were sequenced on
476 Illumina HiSeq4000 sequencers according to the manufacturer's instructions.

477

478 **Hi-C data mapping.**

479 Paired-end .fastq files of Hi-C libraries were aligned and processed using the Juicer package⁷⁴
480 (version 1.5). In brief, each end of the raw reads was mapped separately to the *Mus musculus* mm10
481 reference genome, and Hi-C pairs files were created using BWA⁷⁵ (version 0.7.3a). Mapping statistics are
482 summarized in Supplementary Table 1. .hic files, a highly compressed binary file was created by Juicer
483 tools pre. Matrix balancing was performed with the cooler software package (version 0.8.11) and
484 visualized using the HiCExplorer⁷⁶ (version 3.6) for use with the application hicPlotMatrix. To generate
485 and visualize interaction frequency heat maps of whole chromosomes, Hi-C matrices at 250-kb resolution
486 were imported to the software package HiCExplorer for use with the application hicPlotMatrix. To aid
487 visual comparisons between the datasets, matrices were natural log transformed. To analyze differential
488 interaction frequencies between samples, the HiCExplorer application hicCompareMatrices was used to

489 generate log2 ratios of interaction frequency matrices between two separate datasets and then visualized
490 by hicPlotMatrix.

491

492 **Hi-C: Evaluation of Hi-C biological replicates.**

493 Pearson correlation coefficients between Hi-C biological replicates at each stage were obtained
494 by using the hicCorrelate included in HiCEexplorer using the cool files binned at 10kb with the parameter
495 ‘--log1p --method pearson’. A range from 10kb to 5Mb was used in the calculations. The reproducibility
496 of the results was confirmed with biological replicates (Extended Data Fig. 1c).

497

498 **Hi-C: Contact frequency.**

499 Enrichment of Hi-C counts at different genomic ranges/distances to whole chromosomes was
500 calculated for autosomes and X chromosomes respectively using hicPlotDistVsCounts including
501 HiCEexplorer with the option ‘--maxdepth 300000000’.

502

503 **Hi-C: Identification of chromatin loops.**

504 Chromatin loops were called by using the HiCEexplorer for the use with the application
505 hicDetectLoops using cool files binned at 5kb, 10kb and 25kb respectively with the parameter ‘--
506 maxLoopDistance 2000000’. The cool files were generated from hic files created using only reads with a
507 MAPQ score of 30 or higher using the -q 30 option during Juicer tools pre procedure and converted to
508 cool files using the hicConvertFormat included in HiCEexplorer and the cooler balance included in cooler.
509 After detecting chromatin loops at each resolution, the loops from each resolution were merged by using
510 the hicMergeLoops included in HiCEexplorer with the ‘-r 25000’ option. CTCF, H3K4me3/H3K27ac and
511 H3K27me3-dependent loops were detected using bed files of CTCF (this study),
512 H3K4me3³⁹/H3K27ac^{17,38} or H3K27me3³⁹ ChIP-seq datas by the hicValidateLocations with the ‘--method
513 loops --resolution 25000’ option. Juicer tools compare was used to detect common loops between the two
514 types of chromatin loops, with the option ‘-m 25000 0 mm10’. The loop listed as “Common”, “A” or “B”
515 in parent_list of the output data was used as the common loops between the two loops. IGV⁷⁷ (version
516 2.8.3) was used to visualize chromatin loops in the genomic track view. Genes where the anchor site of
517 the loop overlaps with the TSS region using refTSS_v3.1_mouse_annotation.txt
518 (https://reftss.riken.jp/datafiles/3.1/mouse/gene_annotation/) were identified as a group of genes
519 associated with a specific loop.

520

521 **Hi-C: Identification of Topologically Associated Domains (TADs).**

522 TADs were detected by the hicFindTads including HiCEexplorer using the cool files binned at
523 25kb with the parameter ‘--correctForMultipleTesting fdr --minDepth 80000 --maxDepth 800000 --step

524 40000 minBoundaryDistance 80000 --thresholdComparisons 0.01 --delta 0.01'. TAD boundaries were
525 analyzed by extending 25 kb each upstream and downstream from the TAD boundaries detected by
526 hicFindTads for downstream analysis. CTCF, H3K4me3/H3K27ac and H3K27me3-dependent TAD
527 boundaries were detected using bed files of CTCF, H3K4me3/H3K27ac or H3K27me3 ChIP-seq datas by
528 the hicValidateLocations with the '--method tad --resolution 25000' option. Common TAD boundaries
529 between the two data sets were detected using bedtools intersect, and were assumed to be common if they
530 covered even 1 bp.

531

532 **Hi-C: Identification of mitotic and meiotic specific SEs and genomic sites interacting with meiotic
533 SEs.**

534 The SE files downloaded from Maezawa et al., 2020¹⁷ was used with a modified version of the
535 SE file. The SEs detected in THY1⁺ and KIT⁺, excluding those overlapping with the SEs detected in PS
536 and RS, were used as mitotic specific SEs, and conversely, the SEs detected in PS and RS, excluding
537 those detected in THY1⁺ and KIT⁺, were used as meiotic specific SEs in this study. To determine whether
538 PS chromatin loops overlapped with meiotic SE, the anchor stes of PS chromatin loops were added +0.4
539 Mb upstream and downstream, and it was determined whether this region overlapped with meiotic SE.

540 The regions interacting with meiotic SEs followed the method described in '3.4.6 Identification
541 of super-enhancer-promoter interactions' by Sakashita et al., 2023⁷⁸. The first step in the analysis is to
542 calculate the quality of each viewpoint (SE locus) using the chicQualityControl program including in
543 HiCExplorer, which considers the sparsity of the Hi-C contact frequency with the '--sparsity 0.3' option.
544 Next, using the bed file containing the filtered viewpoints and the program
545 chicViewpointBackgroundModel, a background model of all given viewpoints is calculated based on the
546 Hi-C contact matrix, with the option to set the range of the background model to 500 kb with the '--
547 fixateRange 500000' option. Using the chicViewpoint program, all interaction points in physical contact
548 with the SE locus are detected based on the background model, ranging up to 500 kb (--range 500000
549 500000). Finally, using the chicSignificantInteractions program with the '-p 0.05 --range 500000 500000
550 --loosePValue 0.1', only significant interaction points (P<0.05 (-p 0.05)) were extracted, which were
551 designated as genomic regions interacting with meiotic specific SEs.

552

553 **Hi-C: Pile-up analysis.**

554 Pile-up analysis was performed using coolup.py³⁶ (version 0.9.5) to visualize the average
555 interaction strength of chromatin loops and TADs. Chromatin loops were analyzed using the cool files
556 binned at 10kb resolution and a bedpe file of the corresponding chromatin loops. TAD domains were
557 analyzed using the cool files binned at 25kb resolution and bed file showing TAD domains with the '--
558 rescale --local' option. TAD boundaries were analyzed using the cool files binned at 25kb resolution and

559 bed file showing TAD boundaries with the ‘--pad 500 --local’ option. For the analysis of interactions
560 between mitotic or meiotic SEs, bed files showing mitotic or meiotic SEs were used. For the pile-up
561 analysis showing the interaction among mitotic or mitosis-specific SEs, each SEs were analyzed using the
562 cool files binned at 10kb resolution and bed file showing TAD boundaries with the ‘--pad 500’ option.
563 For the interaction between CTCFs on meiotic SEs, the overlap regions between meiotic SEs and CTCF
564 binding sites in PS were used for analysis. CTCFs on meiotic SEs were analyzed using the cool files
565 binned at 10kb resolution and bed files showing TAD boundaries with the ‘--pad 500’ option. Piled-up
566 data were visualized by performing plotup.py.

567

568 **RNA-seq data analysis.**

569 Row RNA-seq reads after trimming by Sickle (<https://github.com/najoshi/sickle>) (version 1.33)
570 trimmed regions with quality less than 30 and excluded reads that were less than 20 bp. Trimmed
571 sequencing reads were aligned to the *Mus musculus* mm10 reference genome using HISAT2⁷⁹ (version
572 2.2.1) with default parameters. All unmapped reads and non-uniquely mapped reads were filtered out and
573 then sorted by samtools⁸⁰ (version 1.14) with default parameters. The output bam file was assembled and
574 quantified using StringTie⁸¹ (version 2.2.1) based on the mouse gene annotation
575 (gencode.vM25.annotation.gtf). Transcripts per million (TPM) value was used for downstream analyses.

576 Genes associated with *Scml2*-KO PS-specific loops were defined with genes whose TSS regions
577 overlapped with the anchor sites of these loops. Then, only genes with TPM values greater than 1 in any
578 of the cells were extracted and used for analysis. Violinplot was drawn using the R package ggplot2. The
579 log10-transformed values of TPM values+1 were used for statistical analysis and plotting. GO term
580 analysis was performed using the website tool DAVID (<https://david.ncifcrf.gov/home.jsp>). GO term was
581 visualized by ggplot2 of the R package based on gene number, fold enrichment, and *P* value.

582

583 **ChIP-seq data analysis.**

584 Cross-linking ChIP-seq was performed for CTCFs of THY1⁺, WT PS, and *Scml2*-KO PS, using
585 the same methods as previously reported¹⁷. The reproducibility of the results was confirmed with
586 biological replicates (Extended Data Fig. 2a, 3b). Row ChIP-seq reads after trimming by Sickle trimmed
587 regions with quality less than 20 and excluded reads that were less than 20 bp. Trimmed sequencing reads
588 were aligned to the *Mus musculus* mm10 reference genome using Bowtie2⁷⁵ (version 2.4.5) with default
589 parameters. All unmapped reads and non-uniquely mapped reads were filtered out and then sorted by
590 samtools (version 1.14) with default parameters. All unmapped and uniquely mapped reads were filtered
591 out, and sorted by default parameters using samtools, and then ‘MarkDuplicates’ command in Picard tools
592 (version 2.26.9; <https://broadinstitute.github.io/picard/>) was used to remove PCR duplicates by using the
593 option ‘VALIDATION_STRINGENCY=LENIENT ASSUME_SORTED=true

594 REMOVE_DUPLICATES=true'. After this process, the bam files sorted by samtools again were used for
595 downstream analysis.

596 To compare biological replicates, Pearson correlation coefficients were calculated and plotted by
597 multiBamSummary bins and plot correlation from deepTools⁸² (version 3.5.1). For visualization of ChIP-
598 seq using IGC, normalized genome coverage tracks based on counts per million mapped reads were
599 generated as bigwig files using bamCoverage function of deepTools with '--binSize=5 --normalization
600 CPM' parameter. Bigwig files were also used for visualization of ChIP-seq data using IGV. Peak calls
601 were identified using MACS2⁸³ (version 2.2.7.1). The ngs.plot was used to draw tag density and heat
602 maps for read enrichment within \pm 2kb for CTCF and histone modification, \pm 3kb for A-MYB analysis at
603 meiotic SEs interacting sites, and \pm 5kb for A-MYB analysis at anchor sites of PS chromatin loops⁸⁴. A-
604 MYB binding genes were extracted using the online website GREAT (version 4.0.4;
605 <http://great.stanford.edu/public/html/>) for genes with TSS in the peak \pm 2 kb region of A-MYB ChIP-seq.
606

607 **Statistics.**

608 Statistical methods and *P* values for each plot are listed in the figure legends and/or in the
609 Methods. For all experiments, no statistical methods were used to predetermine sample size. Experiments
610 were not randomized, and investigators were not blinded to allocation during experiments and outcome
611 assessments.

613 **Data availability**

614 Hi-C and CTCF ChIP-seq datasets were deposited in the Gene Expression Omnibus under
615 accession no. GSE244681. All other next-generation sequencing datasets used in this study are publicly
616 available. RNA-seq data from THY1⁺ spermatogonia, PS and RS were downloaded from the GEO
617 (accession no. GSE55060). ChIP-seq data for H3K4me2, H3K4me2 and H3K27me3 and RNA-seq data
618 from KIT⁺ spermatogonia were downloaded from the GEO (GSE89502). ChIP-seq data for H3K27ac in
619 WT PS were downloaded from the GEO (GSE107398). H3K27ac in THY1⁺ and KIT⁺ spermatogonia and
620 input for CTCF ChIP-seq were downloaded from the GEO (GSE130652). A-MYB ChIP seq in whole
621 testis was downloaded from GEO (GSE44588). Source data are provided in this paper.

623 **Code availability**

624 Source code for all software and tools used in this study, with documentation, examples, and
625 additional information, is available at the URLs listed above.

627

References

1. Kadauke, S. & Blobel, G.A. Chromatin loops in gene regulation. *Biochim Biophys Acta* **1789**, 17-25 (2009).
2. Holwerda, S. & de Laat, W. Chromatin loops, gene positioning, and gene expression. *Front Genet* **3**, 217 (2012).
3. Zheng, H. & Xie, W. The role of 3D genome organization in development and cell differentiation. *Nat Rev Mol Cell Biol* **20**, 535-550 (2019).
4. Misteli, T. The Self-Organizing Genome: Principles of Genome Architecture and Function. *Cell* **183**, 28-45 (2020).
5. Lieberman-Aiden, E. *et al.* Comprehensive mapping of long-range interactions reveals folding principles of the human genome. *Science* **326**, 289-93 (2009).
6. Stadhouders, R., Filion, G.J. & Graf, T. Transcription factors and 3D genome conformation in cell-fate decisions. *Nature* **569**, 345-354 (2019).
7. Kubo, N. *et al.* Promoter-proximal CTCF binding promotes distal enhancer-dependent gene activation. *Nat Struct Mol Biol* **28**, 152-161 (2021).
8. Olbrich, T. *et al.* CTCF is a barrier for 2C-like reprogramming. *Nat Commun* **12**, 4856 (2021).
9. Griswold, M.D. Spermatogenesis: The Commitment to Meiosis. *Physiol Rev* **96**, 1-17 (2016).
10. Song, H.W. & Wilkinson, M.F. Transcriptional control of spermatogonial maintenance and differentiation. *Semin Cell Dev Biol* **30**, 14-26 (2014).
11. Alavattam, K.G., Maezawa, S., Andreassen, P.R. & Namekawa, S.H. Meiotic sex chromosome inactivation and the XY body: a phase separation hypothesis. *Cell Mol Life Sci* **79**, 18 (2021).
12. Sasaki, K. & Sangrithi, M. Developmental origins of mammalian spermatogonial stem cells: New perspectives on epigenetic regulation and sex chromosome function. *Mol Cell Endocrinol* **573**, 111949 (2023).
13. Lesch, B.J., Dokshin, G.A., Young, R.A., McCarrey, J.R. & Page, D.C. A set of genes critical to development is epigenetically poised in mouse germ cells from fetal stages through completion of meiosis. *Proc Natl Acad Sci U S A* **110**, 16061-6 (2013).
14. Hasegawa, K. *et al.* SCML2 establishes the male germline epigenome through regulation of histone H2A ubiquitination. *Dev Cell* **32**, 574-88 (2015).
15. Sin, H.S., Kartashov, A.V., Hasegawa, K., Barski, A. & Namekawa, S.H. Poised chromatin and bivalent domains facilitate the mitosis-to-meiosis transition in the male germline. *BMC Biol* **13**, 53 (2015).
16. Tomizawa, S.I. *et al.* Kmt2b conveys monovalent and bivalent H3K4me3 in mouse spermatogonial stem cells at germline and embryonic promoters. *Development* **145** (2018).
17. Maezawa, S. *et al.* Super-enhancer switching drives a burst in gene expression at the mitosis-to-meiosis transition. *Nat Struct Mol Biol* **27**, 978-988 (2020).
18. Turner, J.M. Meiotic Silencing in Mammals. *Annu Rev Genet* **49**, 395-412 (2015).
19. Abe, H. *et al.* The Initiation of Meiotic Sex Chromosome Inactivation Sequesters DNA Damage Signaling from Autosomes in Mouse Spermatogenesis. *Curr Biol* **30**, 408-420.e5 (2020).
20. Alavattam, K.G. *et al.* Attenuated chromatin compartmentalization in meiosis and its maturation in sperm development. *Nat Struct Mol Biol* **26**, 175-184 (2019).
21. Vara, C. *et al.* Three-Dimensional Genomic Structure and Cohesin Occupancy Correlate with Transcriptional Activity during Spermatogenesis. *Cell Rep* **28**, 352-367 e9 (2019).
22. Luo, Z. *et al.* Reorganized 3D Genome Structures Support Transcriptional Regulation in Mouse Spermatogenesis. *iScience* **23**, 101034 (2020).
23. Wang, Y. *et al.* Reprogramming of Meiotic Chromatin Architecture during Spermatogenesis. *Mol Cell* **73**, 547-561.e6 (2019).
24. Zuo, W. *et al.* Stage-resolved Hi-C analyses reveal meiotic chromosome organizational features influencing homolog alignment. *Nat Commun* **12**, 5827 (2021).
25. Bolcun-Filas, E. *et al.* A-MYB (MYBL1) transcription factor is a master regulator of male meiosis. *Development* **138**, 3319-30 (2011).

678 26. Maezawa, S., Yukawa, M., Alavattam, K.G., Barski, A. & Namekawa, S.H. Dynamic
679 reorganization of open chromatin underlies diverse transcriptomes during spermatogenesis.
680 *Nucleic Acids Res* **46**, 593-608 (2018).

681 27. Rao, S.S. *et al.* A 3D map of the human genome at kilobase resolution reveals principles of
682 chromatin looping. *Cell* **159**, 1665-80 (2014).

683 28. Bonev, B. *et al.* Multiscale 3D Genome Rewiring during Mouse Neural Development. *Cell* **171**,
684 557-572 e24 (2017).

685 29. Marchal, C. *et al.* High-resolution genome topology of human retina uncovers super enhancer-
686 promoter interactions at tissue-specific and multifactorial disease loci. *Nat Commun* **13**, 5827
687 (2022).

688 30. Fudenberg, G. & Mirny, L.A. Higher-order chromatin structure: bridging physics and biology.
689 *Curr Opin Genet Dev* **22**, 115-24 (2012).

690 31. Dixon, J.R. *et al.* Topological domains in mammalian genomes identified by analysis of
691 chromatin interactions. *Nature* **485**, 376-80 (2012).

692 32. Nora, E.P. *et al.* Spatial partitioning of the regulatory landscape of the X-inactivation centre.
693 *Nature* **485**, 381-5 (2012).

694 33. de Laat, W. & Duboule, D. Topology of mammalian developmental enhancers and their
695 regulatory landscapes. *Nature* **502**, 499-506 (2013).

696 34. Li, Q., Barkess, G. & Qian, H. Chromatin looping and the probability of transcription. *Trends
697 Genet* **22**, 197-202 (2006).

698 35. Furlong, E.E.M. & Levine, M. Developmental enhancers and chromosome topology. *Science*
699 **361**, 1341-1345 (2018).

700 36. Flyamer, I.M., Illingworth, R.S. & Bickmore, W.A. Coolpup.py: versatile pile-up analysis of Hi-
701 C data. *Bioinformatics* **36**, 2980-2985 (2020).

702 37. Bonev, B. & Cavalli, G. Organization and function of the 3D genome. *Nat Rev Genet* **17**, 661-678
703 (2016).

704 38. Adams, S.R. *et al.* RNF8 and SCML2 cooperate to regulate ubiquitination and H3K27 acetylation
705 for escape gene activation on the sex chromosomes. *PLoS Genet* **14**, e1007233 (2018).

706 39. Maezawa, S. *et al.* Polycomb protein SCML2 facilitates H3K27me3 to establish bivalent domains
707 in the male germline. *Proc Natl Acad Sci U S A* **115**, 4957-4962 (2018).

708 40. Li, X.Z. *et al.* An ancient transcription factor initiates the burst of piRNA production during early
709 meiosis in mouse testes. *Mol Cell* **50**, 67-81 (2013).

710 41. Zheng, K. & Wang, P.J. Blockade of pachytene piRNA biogenesis reveals a novel requirement
711 for maintaining post-meiotic germline genome integrity. *PLoS Genet* **8**, e1003038 (2012).

712 42. Zhou, S., Sakashita, A., Yuan, S. & Namekawa, S.H. Retrotransposons in the Mammalian Male
713 Germline. *Sex Dev* **16**, 404-422 (2022).

714 43. Hnisz, D. *et al.* Super-enhancers in the control of cell identity and disease. *Cell* **155**, 934-47
715 (2013).

716 44. Whyte, W.A. *et al.* Master transcription factors and mediator establish super-enhancers at key cell
717 identity genes. *Cell* **153**, 307-19 (2013).

718 45. Pott, S. & Lieb, J.D. What are super-enhancers? *Nat Genet* **47**, 8-12 (2015).

719 46. Zickler, D. & Kleckner, N. Meiotic chromosomes: integrating structure and function. *Annu Rev
720 Genet* **33**, 603-754 (1999).

721 47. Dowen, J.M. *et al.* Control of cell identity genes occurs in insulated neighborhoods in mammalian
722 chromosomes. *Cell* **159**, 374-387 (2014).

723 48. Li, M. *et al.* Comprehensive 3D epigenomic maps define limbal stem/progenitor cell function and
724 identity. *Nat Commun* **13**, 1293 (2022).

725 49. Namekawa, S.H. *et al.* Postmeiotic sex chromatin in the male germline of mice. *Curr Biol* **16**,
726 660-7 (2006).

727 50. Ichijima, Y. *et al.* MDC1 directs chromosome-wide silencing of the sex chromosomes in male
728 germ cells. *Genes Dev* **25**, 959-71 (2011).

729 51. Patel, L. *et al.* Dynamic reorganization of the genome shapes the recombination landscape in
730 meiotic prophase. *Nat Struct Mol Biol* **26**, 164-174 (2019).

731 52. Barski, A. *et al.* Pol II and its associated epigenetic marks are present at Pol III-transcribed
732 noncoding RNA genes. *Nat Struct Mol Biol* **17**, 629-34 (2010).

733 53. Ernst, C. & Jefri, M. Epigenetic priming in neurodevelopmental disorders. *Trends Mol Med* **27**,
734 1106-1114 (2021).

735 54. Vicente-Duenas, C., Hauer, J., Cobaleda, C., Borkhardt, A. & Sanchez-Garcia, I. Epigenetic
736 Priming in Cancer Initiation. *Trends Cancer* **4**, 408-417 (2018).

737 55. Jin, F. *et al.* A high-resolution map of the three-dimensional chromatin interactome in human
738 cells. *Nature* **503**, 290-4 (2013).

739 56. Ghavi-Helm, Y. *et al.* Enhancer loops appear stable during development and are associated with
740 paused polymerase. *Nature* **512**, 96-100 (2014).

741 57. Rubin, A.J. *et al.* Lineage-specific dynamic and pre-established enhancer-promoter contacts
742 cooperate in terminal differentiation. *Nat Genet* **49**, 1522-1528 (2017).

743 58. Ji, X. *et al.* 3D Chromosome Regulatory Landscape of Human Pluripotent Cells. *Cell Stem Cell*
744 **18**, 262-75 (2016).

745 59. Alexander, A.K. *et al.* A-MYB and BRDT-dependent RNA Polymerase II pause release
746 orchestrates transcriptional regulation in mammalian meiosis. *Nat Commun* **14**, 1753 (2023).

747 60. Sabari, B.R. *et al.* Coactivator condensation at super-enhancers links phase separation and gene
748 control. *Science* **361**(2018).

749 61. Shang, E., Nickerson, H.D., Wen, D., Wang, X. & Wolgemuth, D.J. The first bromodomain of
750 Brdt, a testis-specific member of the BET sub-family of double-bromodomain-containing
751 proteins, is essential for male germ cell differentiation. *Development* **134**, 3507-15 (2007).

752 62. Ishikura, Y. *et al.* In vitro reconstitution of the whole male germ-cell development from mouse
753 pluripotent stem cells. *Cell Stem Cell* **28**, 2167-2179.e9 (2021).

754 63. Culty, M. Gonocytes, the forgotten cells of the germ cell lineage. *Birth Defects Res C Embryo*
755 *Today* **87**, 1-26 (2009).

756 64. Manku, G. & Culty, M. Mammalian gonocyte and spermatogonia differentiation: recent advances
757 and remaining challenges. *Reproduction* **149**, R139-57 (2015).

758 65. Yamanaka, S. *et al.* Broad Heterochromatic Domains Open in Gonocyte Development Prior to De
759 Novo DNA Methylation. *Dev Cell* **51**, 21-34 e5 (2019).

760 66. Nagano, M. *et al.* Nucleome programming is required for the foundation of totipotency in
761 mammalian germline development. *EMBO J* **41**, e110600 (2022).

762 67. Hore, T.A., Deakin, J.E. & Marshall Graves, J.A. The evolution of epigenetic regulators CTCF
763 and BORIS/CTCFL in amniotes. *PLoS Genet* **4**, e1000169 (2008).

764 68. Loukinov, D.I. *et al.* BORIS, a novel male germ-line-specific protein associated with epigenetic
765 reprogramming events, shares the same 11-zinc-finger domain with CTCF, the insulator protein
766 involved in reading imprinting marks in the soma. *Proc Natl Acad Sci U S A* **99**, 6806-11 (2002).

767 69. Rivero-Hinojosa, S. *et al.* The combined action of CTCF and its testis-specific paralog BORIS is
768 essential for spermatogenesis. *Nat Commun* **12**, 3846 (2021).

769 70. Moens, P.B. & Pearlman, R.E. Chromatin organization at meiosis. *Bioessays* **9**, 151-3 (1988).

770 71. Sin, H.S. *et al.* RNF8 regulates active epigenetic modifications and escape gene activation from
771 inactive sex chromosomes in post-meiotic spermatids. *Genes Dev* **26**, 2737-48 (2012).

772 72. Bonora, G. *et al.* Orientation-dependent Dzx4 contacts shape the 3D structure of the inactive X
773 chromosome. *Nat Commun* **9**, 1445 (2018).

774 73. Sakashita, A. *et al.* Endogenous retroviruses drive species-specific germline transcriptomes in
775 mammals. *Nat Struct Mol Biol* **27**, 967-977 (2020).

776 74. Durand, N.C. *et al.* Juicer Provides a One-Click System for Analyzing Loop-Resolution Hi-C
777 Experiments. *Cell Syst* **3**, 95-8 (2016).

778 75. Li, H. & Durbin, R. Fast and accurate short read alignment with Burrows-Wheeler transform.
779 *Bioinformatics* **25**, 1754-60 (2009).

780 76. Ramirez, F. *et al.* High-resolution TADs reveal DNA sequences underlying genome organization
781 in flies. *Nat Commun* **9**, 189 (2018).

782 77. Thorvaldsdottir, H., Robinson, J.T. & Mesirov, J.P. Integrative Genomics Viewer (IGV): high-
783 performance genomics data visualization and exploration. *Brief Bioinform* **14**, 178-92 (2013).

784 78. Sakashita, A., Takeuchi, C., Maezawa, S. & Namekawa, S.H. Bioinformatics Pipelines for
785 Identification of Super-Enhancers and 3D Chromatin Contacts. *Methods Mol Biol* **2577**, 123-146
786 (2023).

787 79. Kim, D., Paggi, J.M., Park, C., Bennett, C. & Salzberg, S.L. Graph-based genome alignment and
788 genotyping with HISAT2 and HISAT-genotype. *Nat Biotechnol* **37**, 907-915 (2019).

789 80. Li, H. *et al.* The Sequence Alignment/Map format and SAMtools. *Bioinformatics* **25**, 2078-9
790 (2009).

791 81. Pertea, M. *et al.* StringTie enables improved reconstruction of a transcriptome from RNA-seq
792 reads. *Nat Biotechnol* **33**, 290-5 (2015).

793 82. Ramírez, F., Dündar, F., Diehl, S., Grüning, B.A. & Manke, T. deepTools: a flexible platform for
794 exploring deep-sequencing data. *Nucleic Acids Res* **42**, W187-91 (2014).

795 83. Zhang, Y. *et al.* Model-based analysis of ChIP-Seq (MACS). *Genome Biol* **9**, R137 (2008).

796 84. Shen, L., Shao, N., Liu, X. & Nestler, E. ngs.plot: Quick mining and visualization of next-
797 generation sequencing data by integrating genomic databases. *BMC Genomics* **15**, 284 (2014).

798

799 **Acknowledgments**

800 We thank members of the Namekawa lab, Kris Alavattam, Brad Cairns, and Chongil Yi for the
801 discussion, Xin Li for sharing *A-myb* mutant mice, and Artem Barski for sharing the reagents.

802 **Funding**

803 JSPS Overseas Challenge Program for Young Researchers, TOYOBO Biotechnology Foundation and
804 JSPS Overseas Research Fellowship to Y.K. NIH Grants GM122776 and GM141085 to S.H.N.

806 **Author contributions**

807 Y.K. and S.H.N. designed the study. K.T. and S.M performed experiments. Y.K. performed the
808 computational analyses. Y.M. contributed to the computational analyses. A.S. contributed to developing a
809 computational tool. Y.K., N.K, and S.H.N interpreted the computational analyses. Y.K. and S.H.N. wrote
810 the manuscript with critical feedback from all other authors. S.H.N. supervised the project.

811 **Competing interest statement**

812 The authors declare no competing interests.

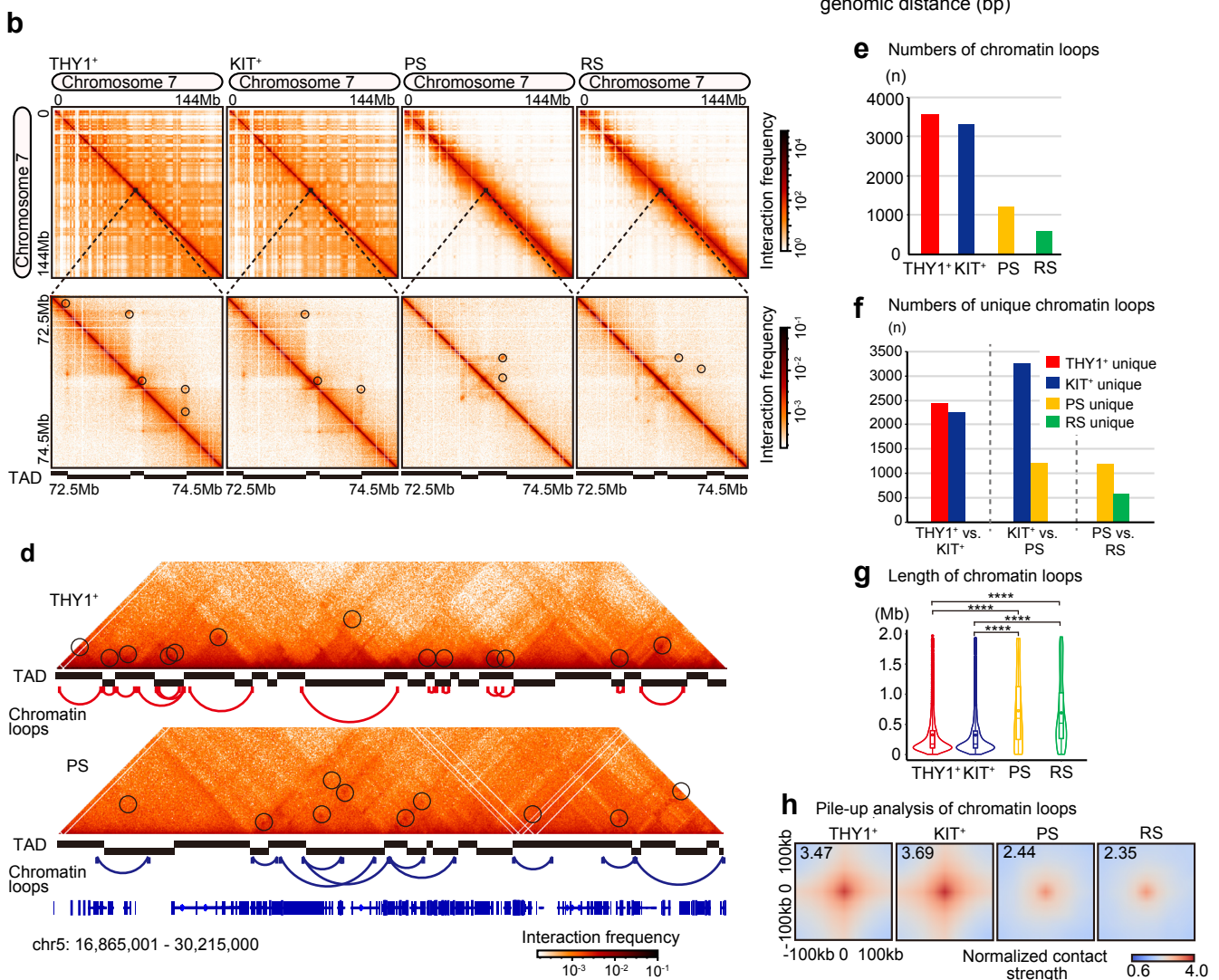
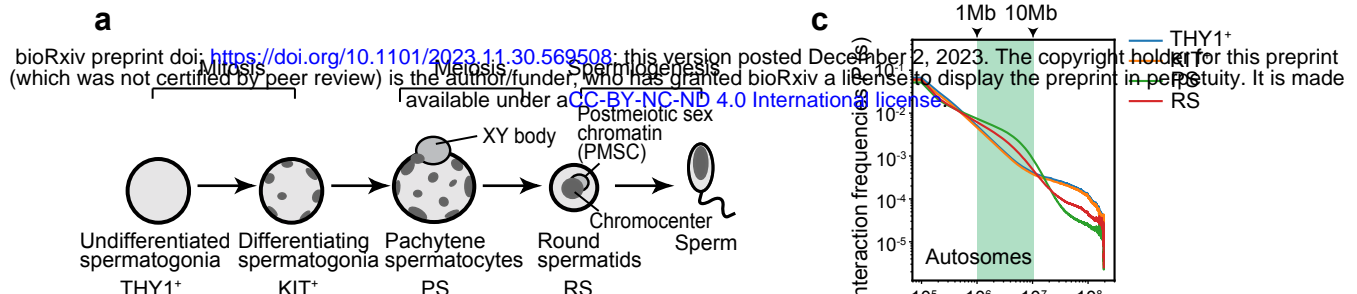


Figure 1. 3D chromatin reprogramming and inter-TAD chromatin loop formation in meiosis.

a, Schematic of the stages of mouse spermatogenesis analyzed in this study. THY1⁺: undifferentiated spermatogonia; KIT⁺: differentiating spermatogonia; PS: pachytene spermatocytes; RS: round spermatids.

b, Hi-C maps showing normalized Hi-C interaction frequencies (100kb bins, chromosome 7) in THY1⁺, KIT⁺, PS, and RS. 10kb bins normalized Hi-C matrices were used for the zoom-in. Black circles in the Hi-C map indicate chromatin loops.

c, Hi-C interaction frequency probabilities P stratified by genomic distance s for each cell type shown (100kb bins). All autosomes were analyzed.

d, Hi-C interaction heatmaps (25kb bins, chromosome 5, 16,865,001-30,215,000bp) in THY1⁺ and PS. Chromatin loops are indicated by black circles, red lines in THY1⁺, and blue lines in PS.

e, Numbers of chromatin loops (n) detected from each Hi-C data set (merged results for each using 5kb, 10kb, and 25kb bin data).

f, Numbers of unique chromatin loops comparing each pairwise developmental stage.

g, Chromatin loop length (Mb) from each Hi-C data set (merged results for each using 5kb, 10kb, and 25kb bin data). The number of loops used in the analysis was equal to the number shown in e (THY1⁺: $n=3,562$, KIT⁺: $n=3,336$, PS: $n=1,223$, RS: $n=609$). The box indicates the 25th, median and 75th percentiles, and the dot in the box indicates mean. Statistical analysis is based on Bonferroni correction. **** indicates $p < 2e^{-16}$.

h, Chromatin loop pile-up in each cell type with 100kb padding. Color represents normalized contact strength in the log scale. The normalized contact strength values in the central pixel are shown on the top left.

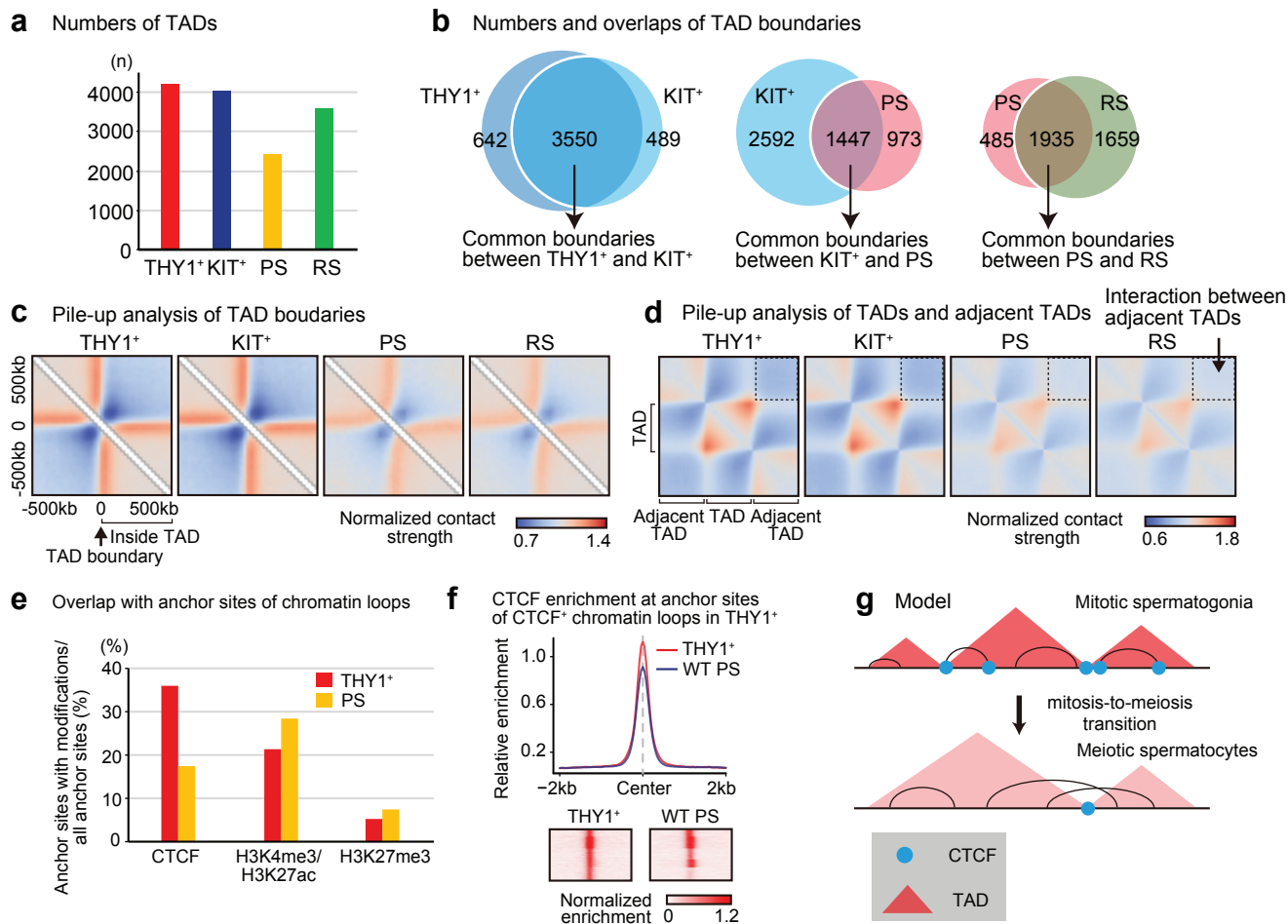


Figure 2. TAD and chromatin loop reorganization during spermatogenesis.

- a**, Numbers of TADs (n) detected from each Hi-C data set (25kb bins).
- b**, Venn diagram showing numbers and overlaps of TAD boundaries in each developmental stage.
- c**, Local pile-up analysis of TAD boundaries in each cell type. 10kb bins Hi-C data with 500 kb padding around the central pixel. Color represents normalized contact strength in the log scale.
- d**, Local rescaled pile-ups of TADs from 10kb bin Hi-C data in each cell type. The dotted regions represent interactions between adjacent TADs.
- e**, Ratio of accumulation of CTCF, H3K4me3/H3K27ac, or H3K27me3 at the anchor sites of chromatin loops in THY1⁺ and PS.
- f**, CTCF enrichment at anchor sites of CTCF-dependent chromatin loops in THY1⁺ (detected in panel **e**, 2,532 sites). Heatmaps for each locus are shown at the bottom.
- g**, Model showing TAD and chromatin loop reorganization at the mitosis-to-meiosis transition.

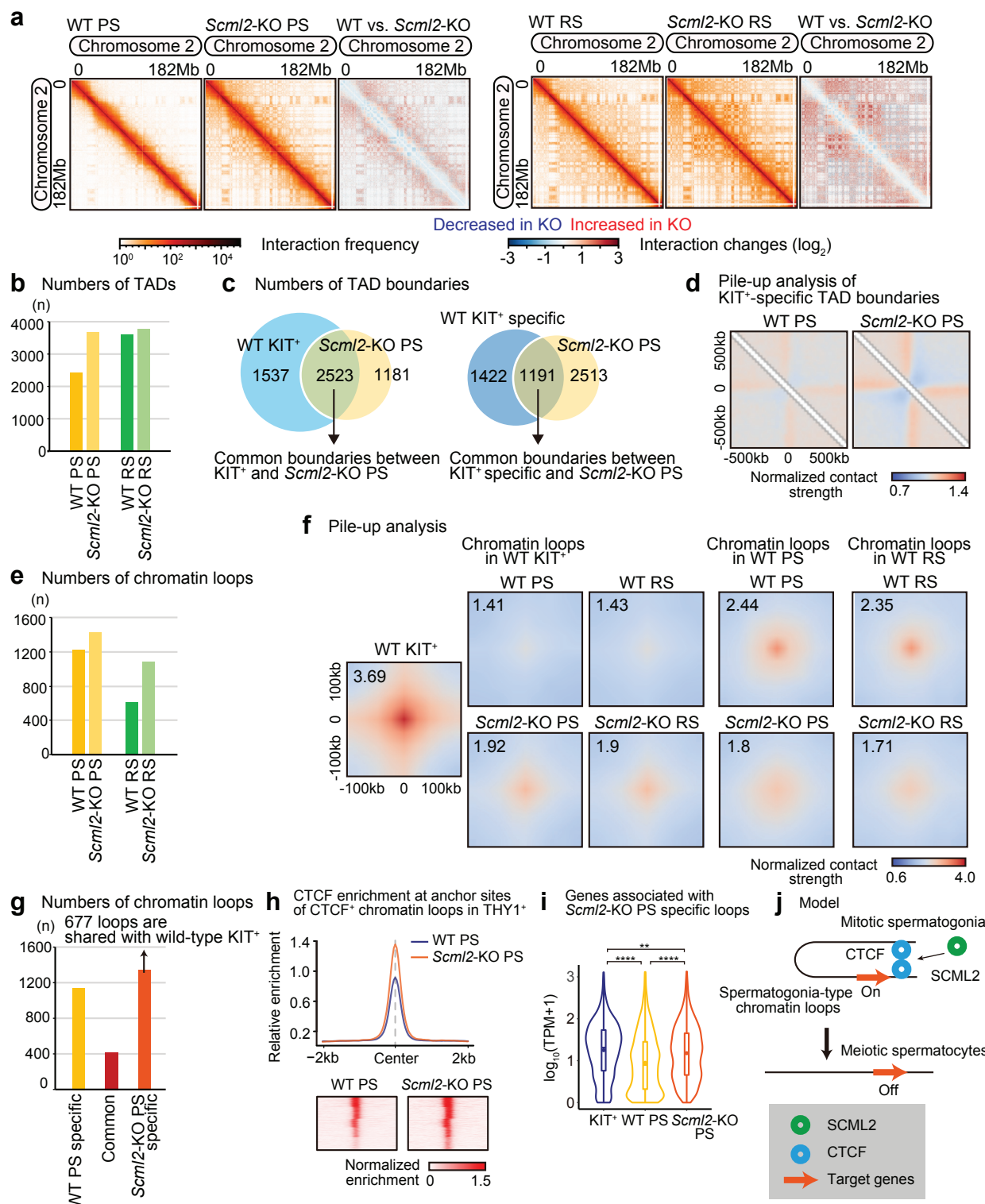


Figure 3. SCML2 is required for the resolution of spermatogonia-type 3D chromatin.

a, Heat maps showing normalized Hi-C interaction frequencies (100kb bins, chromosome 2) in wildtype (WT) PS, *Scml2*-KO PS (left), and WT RS and *Scml2*-KO RS (right). Red and blue Hi-C maps represent a log2 ratio comparison of Hi-C interaction frequencies between WT and *Scml2*-KO.

b, Numbers of TADs (n) detected from each Hi-C data set (25kb bins) in WT PS, *Scml2*-KO PS, WT RS, and *Scml2*-KO RS.

c, Venn diagram showing the overlap between all KIT⁺ TAD boundaries and *Scml2*-KO PS TAD boundaries (left), and the overlap between KIT⁺-specific TAD boundaries and *Scml2*-KO PS TAD boundaries (right). KIT⁺-specific boundaries are defined by excluding TAD boundaries detected in WT PS.

d, Local pile-up analysis of KIT⁺ specific TAD boundaries in WT PS and *Scml2*-KO PS.

e, Numbers of chromatin loops (n) detected in each Hi-C data set (merged results for each using 5kb, 10kb, and 25kb bin data) in WT PS, *Scml2*-KO PS, WT RS, and *Scml2*-KO RS.

f, Chromatin loop pile-up analysis in each cell type with 100kb padding. The normalized contact strength in the central pixel is displayed on the top left.

g, Numbers of specific and common chromatin loops between WT PS and *Scml2*-KO PS. 677 *Scml2*-KO PS-specific loops overlapped with loops detected in KIT⁺. Overlapping loops were detected by Juicer.

h, CTCF enrichment in WT PS and *Scml2*-KO PS at the anchor site of CTCF-chromatin loops in THY1⁺ spermatogonia.

i, Violin plots of RNA-seq reads converted to log10 (TPM+1) value for genes associated with *Scml2*-KO PS specific loops in KIT⁺, WT PS and *Scml2*-KO PS. 1,243 genes were identified by extracting genes present in the anchor site of *Scml2*-KO PS-specific loops. The box indicates the 25th, median and 75th percentiles, and the dot in the box indicates mean. Statistical analysis is based on Bonferroni correction. ****: $p < 2e^{-16}$, **: $p < 0.005$.

j, Model of resolution of spermatogonia-type 3D chromatin by SCML2.

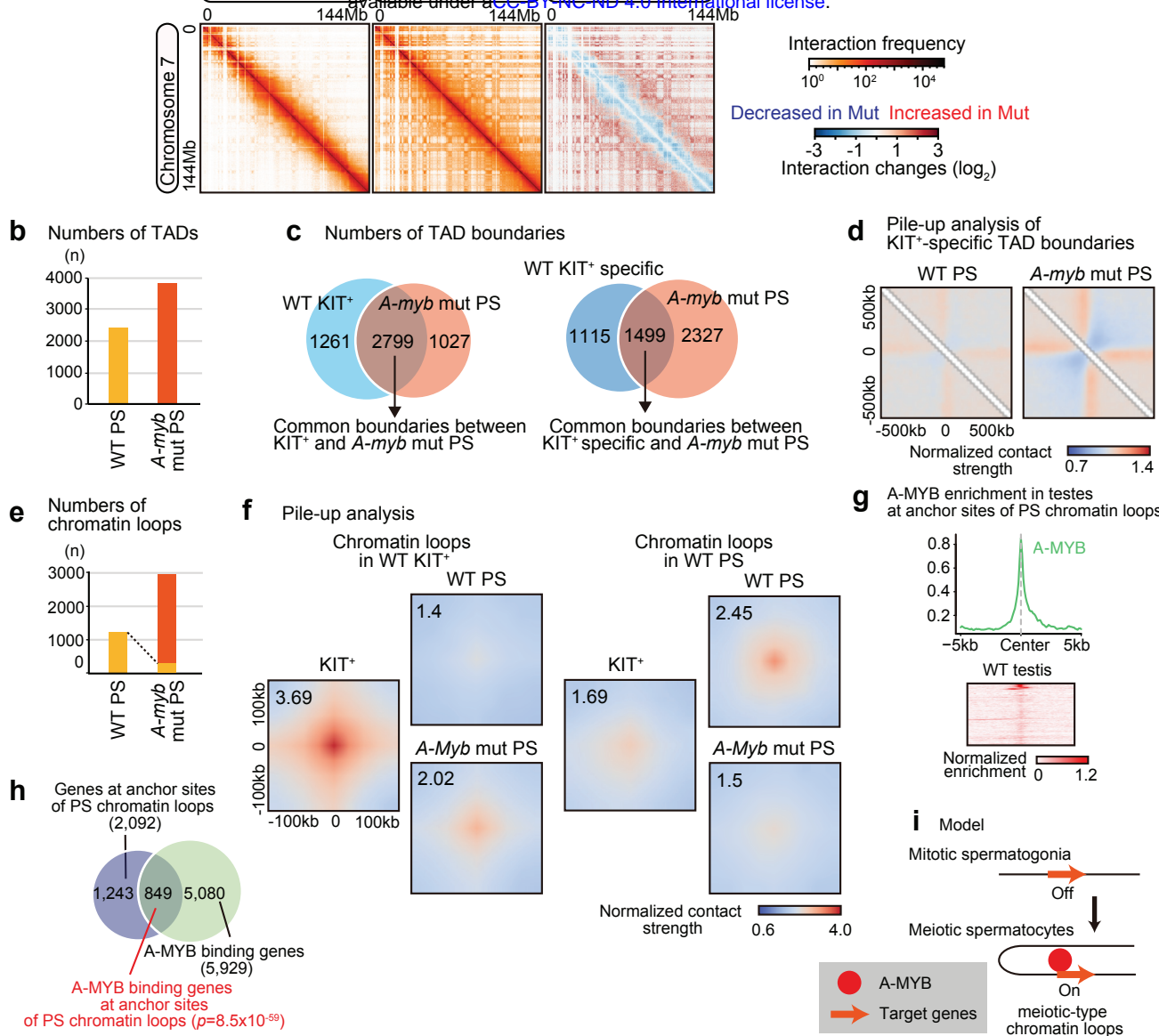


Figure 4. A-MYB is required for the formation of meiotic-type 3D chromatin.

a, Heat maps showing normalized Hi-C interaction frequencies (100kb bins, chromosome 7) in WT PS, *A-myb* mutant PS (left). Red and blue Hi-C maps represent a log₂ ratio comparison of Hi-C interaction frequencies between wild-type and *A-myb* mutant PS.

b, Number of TADs (n) detected from each Hi-C data set (25kb bins) in WT PS and *A-myb* mutant PS.

c, Venn diagram showing the overlap between all KIT⁺ TAD boundaries and *A-myb* mutant PS TAD boundaries (left), and the overlap between KIT⁺-specific TAD boundaries and *A-myb* mutant PS TAD boundaries (right). KIT⁺-specific boundaries are defined by excluding boundaries detected in WT PS.

d, Local pile-up analysis of KIT⁺-specific TAD boundaries in WT PS and *A-myb* mutant PS.

e, Number of chromatin loops (n) detected in each Hi-C data set (merged results for each using 5kb, 10kb, and 25kb bin data) in WT PS and *A-myb* mutant PS. Yellow area in the graph of *A-myb* mutant PS indicate that the same loops are detected in WT PS (357 loops).

f, Chromatin loop pile-up analysis in each cell type with 100kb padding. The normalized contact strength in the central pixel is displayed on the top left.

g, ChIP-seq data for A-MYB using whole testis at the regions adjacent to TSS of 849 genes that overlap with anchor sites of chromatin loops in PS.

h, Venn diagram showing the intersection of genes located at anchor sites of chromatin loops in PS (blue) and all A-MYB bound genes (green). The overlap is statistically significant ($p=8.5 \times 10^{-59}$) compared to the proportion of all A-MYB bound genes to all RefSeq genes based on the hypergeometric test.

i, Model of the establishment of meiotic-type chromatin loops by A-MYB.

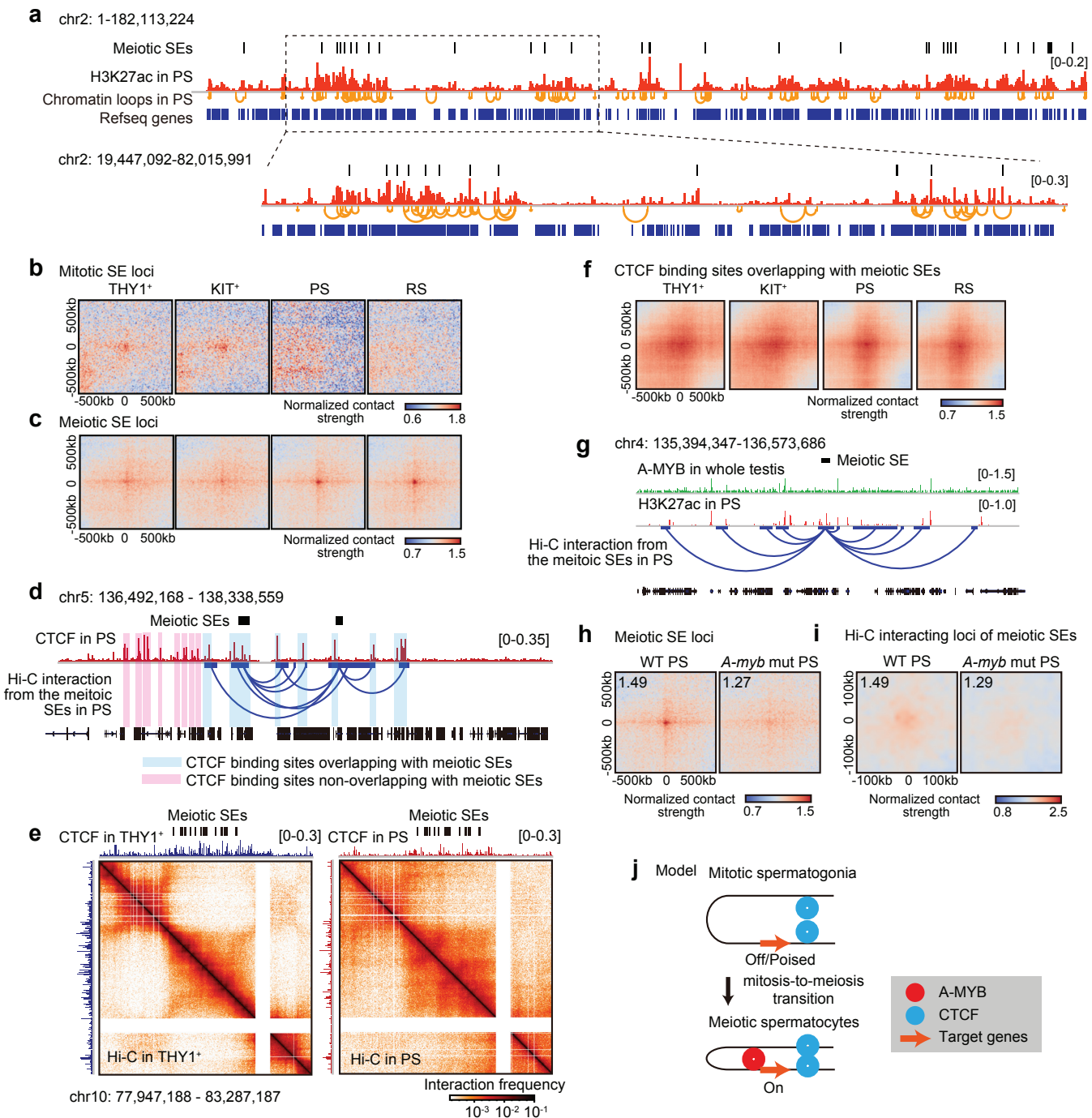


Figure 5. Meiotic super-enhancers are poised with 3D chromatin.

a, Track view showing meiotic SEs, H3K27ac, and chromatin loops in PS on the entire chromosome 2 (top). Enlargement of the boxed area is shown below.

b, Pile-up analysis of averaged intersections of mitotic SEs with 500kb paddles.

c, Pile-up analysis of averaged intersections of meiotic SEs with 500kb paddles.

d, Track view showing CTCF distribution and Hi-C interactions of the meiotic SEs in PS on a region of chromosome 5. Pink highlights indicate CTCF binding sites that do not overlap with meiotic SEs; blue highlights indicate CTCF binding sites that overlap with meiotic SEs and their loops.

e, CTCF binding and Hi-C maps of THY1⁺ spermatogonia and PS around meiotic SEs (25kb bins, chr10: 77,947,188-83,287,187).

f, Pile-up analysis showing average interactions of CTCF binding sites overlapping with meiotic SEs. The pile-up analysis in THY1⁺, KIT⁺, PS, and RS is based on the Hi-C data from each developmental stage and the genomic coordinates of the CTCF binding sites that overlapped with meiotic SEs or their interacting genomic regions.

g, Track view showing the distributions of A-MYB binding and H3K27ac around meiotic SEs. Hi-C interaction from the meiotic SEs is also shown.

h, Pile-up analysis showing average interactions of meiotic SEs with 500kb paddles in WT PS and *A-myb* mutant PS. The normalized contact strength in the central pixel is displayed on the top left.

i, Pile-up analysis showing average interactions of loci that interacted with meiotic SEs based on Hi-C data with 100kb paddles in WT PS and *A-myb* mutant PS.

j, Model of the predetermination of 3D chromatin at meiotic SE loci via CTCF in mitotic spermatogonia. A-MYB strengthens these 3D contacts in meiotic spermatocytes.

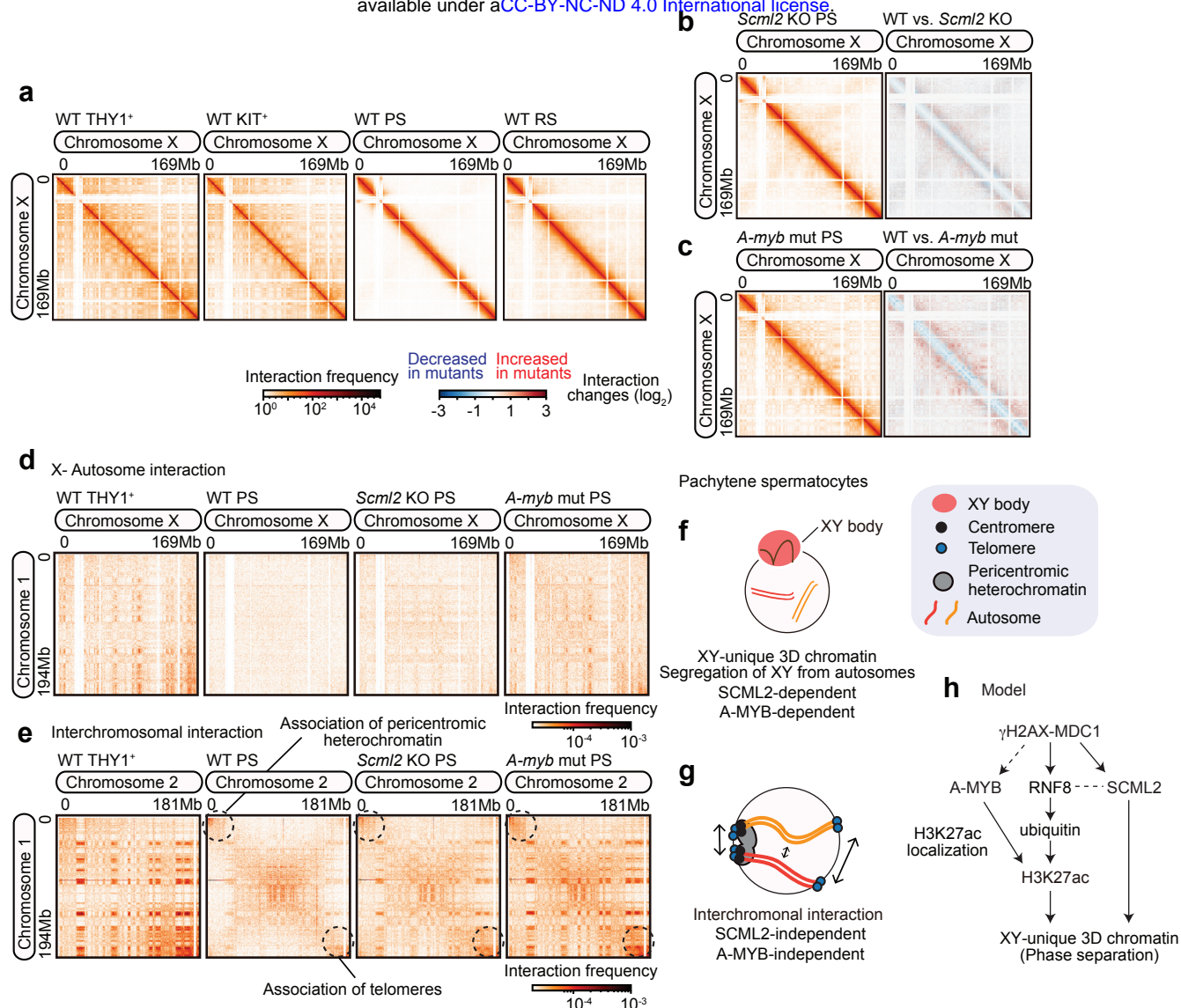


Figure 6. SCML2 and A-MYB establish unique 3D chromatin of the meiotic sex chromosomes

a, Hi-C maps of the X chromosome showing normalized Hi-C interaction frequencies (100kb bins) in WT THY1⁺, KIT⁺, PS, and RS.

b, Heat maps showing normalized Hi-C interaction frequencies (100kb bins, chromosome X) in Scml2-KO PS (left). Red and blue Hi-C maps represent a log2 ratio comparison of Hi-C interaction frequencies between wild-type and Scml2-KO PS (right).

c, Heat maps showing normalized Hi-C interaction frequencies (100kb bins, chromosome X) in A-myb mutant PS (left). Red and blue Hi-C maps represent a log2 ratio comparison of Hi-C interaction frequencies between wild-type and A-myb mutant PS (right).

d, Heat maps showing normalized Hi-C interchromosomal interactions (250-kb bins, chromosomes 1 and X) for WT THY1⁺, WT PS, Scml2-KO PS and A-myb mutant PS.

e, Heat maps showing normalized Hi-C interchromosomal interactions (250-kb bins, chromosomes 1 and 2) for WT THY1⁺, WT PS, Scml2-KO PS and A-myb mutant PS.

f, Model for the establishment of a unique 3D chromatin in the XY body and segregation of XY from autosomes in PS.

g, Model of interchromosomal interactions in pachytene spermatocytes.

h, Schematic of the molecular pathway that establishes a XY-unique 3D chromatin in pachytene spermatocytes.

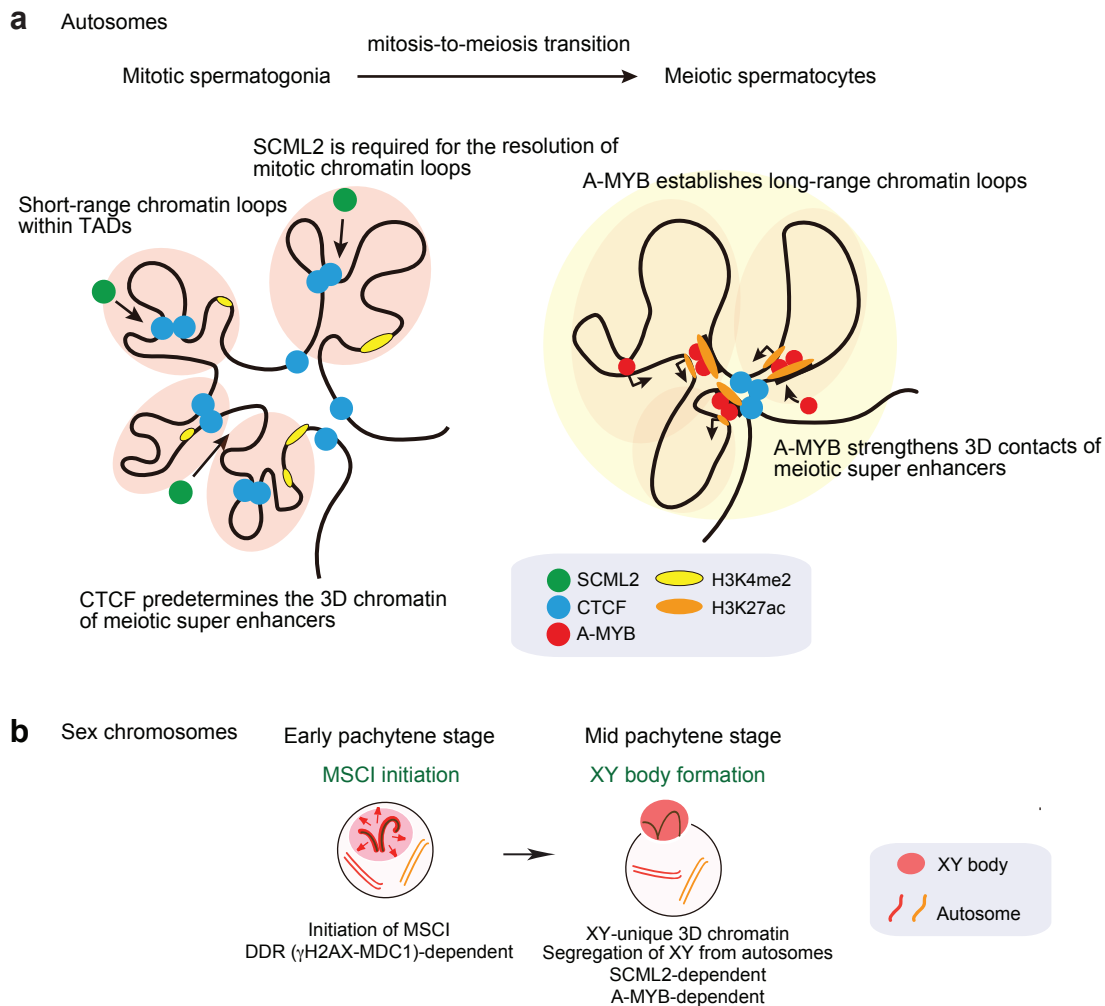


Figure 7. Models of 3D chromatin dynamics and gene regulation on autosomes and sex chromosomes during spermatogenesis.

a, Model showing the changes in chromosome interactions from mitotic spermatogonia to meiotic spermatocytes on autosomes.

b, Model of 3D chromatin dynamic on the sex chromosomes. At the onset of MSCI at the early-pachytene stage, DDR initiated MSCI and, subsequently, SCML2 and A-MYB establish unique 3D chromatin of the sex chromosomes and segregate the sex chromosomes from autosomes at the mid-pachytene stage.